Comprehensive Solid-State Characterization of Rare Earth Fluoride Nanoparticles

Bryan E.G. Lucier,[1] Karen E. Johnston,[1] Donna C. Arnold,[2]

Jean-Luc Lemyre,[3] Ariane Beaupré,[3] Maxime Blanchette,[3]

Anna M. Ritcey,[3] and Robert W. Schurko[1,*]

[1] *Department of Chemistry and Biochemistry, University of Windsor,*

Windsor, Ontario, Canada, N9B 3P4

[2] *University of Kent, School of Physical Sciences, Canterbury, Kent, United Kingdom, CT2 7NH*

[3] *Department of Chemistry and CERMA, Université Laval, Québec, Canada, G1V 0A6*

* To whom correspondence should be addressed.

Phone: 519-253-3000 x3548 Fax: 519-973-7098, E-mail: rschurko@uwindsor.ca

Abstract

The combination of multinuclear solid-state NMR and powder X-ray diffraction has been applied to characterize the octahedron-shaped crystalline nanoparticle products resulting from an inverse micelle synthesis. Rietveld refinements of the powder X-ray diffraction data from the nanoparticles reveal their general formula to be $(H_3O)Y_3F_{10} \bullet xH_2O$. ^{1}H magic-angle spinning (MAS) NMR experiments provide information on sample purity, as well as serving as an excellent probe of the zeolithic incorporation of atmospheric water. ^{19}F MAS NMR experiments on a series of monodisperse nanoparticle samples of various sizes yield spectra featuring three unique ^{19}F resonances, arising from three different fluorine sites within the $(H_3O)Y_3F_{10} \bullet xH_2O$ crystal structure. Partial removal of zeolithic water from the internal cavities and tunnels of the nanoparticles leads to changes in the integrated peak intensities in the ^{19}F MAS NMR spectra; the origin of this behaviour is discussed in terms of ^{19}F longitudinal relaxation. ^{19}F-^{89}Y variable-amplitude cross-polarization (VACP) NMR experiments on both stationary samples and samples under conditions of MAS indicate that two distinct yttrium environments are present, and based on the relative peak intensities, the populations of one of the two sites is closely linked to nanoparticle size. Both ^{19}F MAS and ^{19}F-^{89}Y VACP/MAS experiments indicate small amounts of an impurity present in certain nanoparticles; these are postulated to be spherical amorphous YF_3 nanoparticles. We discuss the importance of probing molecular-level structure in addition to microscopic structure, and how the combination of these characterization methods is crucial for understanding nanoparticle design, synthesis, and application.

Keywords: nanoparticles, zeolite, solid-state NMR, powder X-ray diffraction, ^{19}F NMR, ^{89}Y NMR, characterization

Introduction

Nanoparticles (NPs), small clusters of atoms with dimensions on the order of 10^{-9} to 10^{-7} m, exhibit a wide array of unique properties not observed in bulk materials. As such, NPs are intensively studied, in large part due to their potential applications in bioimaging, drug delivery, and optics.[1-6] Many NPs contain rare earth[7-9] and lanthanide[10-19] elements, which are important for their contributions to the composition and structural makeup of the NP, as well as novel physicochemical behaviour (*e.g.*, enhanced optical properties). Recently, the preparation of yttrium fluoride (YF_3)-based NPs *via* an inverse micelle process was reported,[20,21] with an exceptional level of control exhibited over the size, shape, and crystallinity of the final products. These NPs have octahedral shapes, and their electron diffraction patterns do not match that of bulk YF_3, indicating that different solid phases are formed during their synthesis.[20] The combination of physical (size, shape) and chemical (phase, crystallinity) control over the product afforded by this NP synthesis naturally presents a variety of possible applications for rare earth and lanthanide fluoride-based NPs.[22-28]

NPs are typically characterized by electron microscopy and UV-Vis spectroscopy. The former technique yields information regarding the size and morphology of NPs, whereas the latter sheds light upon the molecular/atomic origins of optical properties. Powder X-ray diffraction (pXRD) methods are also often used to characterize crystalline NPs and offer the opportunity for determination of the crystal space group, and in some cases, the unit cell parameters and associated crystal structure.[29-39] In the case of partially or fully amorphous NPs, pXRD can provide some useful data regarding crystallinity and NP size, but information pertaining to the long-range structure and atomic bonding/interactions is generally unavailable.

Solid-state nuclear magnetic resonance (SSNMR) experiments are often employed to study NPs, providing information on the molecular-level structure,[40-44] short- and long-range order,[45-48] core/shell interfaces,[49-52] ligand/NP interactions,[53-57] and dopants.[58-61] In particular, ^{1}H and ^{13}C SSNMR experiments are routinely applied to study the nature of stabilizing organic surface ligands on inorganic NPs. The structures of NPs with inorganic cores can be further probed if there are nuclides present that are amenable to study by NMR spectroscopy. ^{19}F and ^{89}Y are both spin-1/2 nuclei, 100% naturally abundant, and possess moderate chemical shift ranges. ^{19}F is highly receptive,[62,63] whereas ^{89}Y is unreceptive due to its low gyromagnetic ratio. Furthermore, ^{89}Y SSNMR experiments utilizing direct excitation suffer from poor signal-to-noise ratios (S/N), due not only to the low γ, but also to typically lengthy longitudinal relaxation times ($T_1(^{89}Y)$);[64] hence, ^{89}Y NMR spectra are often acquired using cross-polarization (CP) methods.

Herein, we present a comprehensive SSNMR and pXRD study of crystalline YF_3-based NPs, in order to study the NP composition as well as the molecular-level structures of their cores and surfaces. Powder XRD experiments and Rietveld refinements are used to identify the structure of the unknown phase of the crystalline octahedral NPs. ^{89}Y and ^{19}F SSNMR experiments on NPs of varying size are utilized to examine the unique Y and F environments, and the corresponding NMR resonances are correlated to crystallographic sites. ^{1}H and ^{19}F NMR experiments are used to probe the interactions between water molecules and the NP surfaces, and ^{1}H and ^{13}C NMR are used to study the stabilizing surface ligands. Finally, we discuss the value of an intimate knowledge of NP structure and composition, and its relation to synthetic methods and starting materials, which is essential for the future rational design of NPs with controllable and tunable bulk properties.

Experimental

Synthesis of single crystal $(H_3O)Y_3F_{10} \bullet xH_2O$ nanoparticles. All chemicals were supplied by Sigma Aldrich and used without further purification. Octahedral NPs of different sizes were prepared using variations of a previously described method.[20] The general procedure consists of the addition of aqueous fluoride to a solution of YCl_3 dispersed within reverse micelles, which frequently results in a mixture of particle populations that differ in shape or crystallinity. In order to facilitate spectral analysis, synthetic conditions were selected so as to maximize the production of a uniform population of monodisperse octahedral $(H_3O)Y_3F_{10} \bullet xH_2O$ NPs. The reagent quantities are reported as absolute values, rather than concentrations, because the resultant particle size depends slightly on the overall volume of solution (Table 1). NPs doped with 5% scandium were also prepared (Supporting Information, Figure S1). For each sample, reverse microemulsions were prepared by mixing an aqueous solution of YCl_3, cyclohexane and the surfactants polyoxyethylene(5)nonylphenylether (Igepal CO520) and sodium bis(2-ethylhexyl)sulfosuccinate (AOT). Microemulsions were homogenized with a magnetic stirrer followed by 10 minutes in an ultrasonic bath. An aqueous solution of NH_4HF_2 was then added directly to the microemulsion, with vigorous stirring under ambient conditions. Stirring was maintained over a week to ensure completion of particle growth. The resulting suspensions of $(H_3O)Y_3F_{10} \bullet xH_2O$ nanocrystals appeared clear and were deposited directly on TEM grids. NPs for NMR analysis were isolated from the microemulsions by evaporation of the cyclohexane, dissolution in methanol and centrifugation. Soluble counterions and surfactants were removed by four dispersion/centrifugation cycles using water alternately with methanol. The precipitated NPs were then allowed to dry overnight in an oven at a temperature of 90 °C. The resulting white powders were used for NMR measurements.

Table 1. Synthetic parameters for $(H_3O)Y_3F_{10} \bullet xH_2O$ nanoparticle samples.

Particle Size (nm) [a]	Cyclohexane Volume (mL)	Igepal Mass (g)	AOT Mass (g)	Aqueous Volume [b] (mL)	$[YCl_3(aq)]$ [c] (mmol/L)
21	450	60	-	12	40
37	450	54	6	15	40
67	90	10.8	1.2	3	500
132 [d]	90	3	-	3	500
49	450	54	6	15	38 [e]
83	300	36	4	10	400

[a] The octahedral particle sizes reported in this paper refer to length of the octahedron edge. See text for details. [b] The volume of aqueous NH_4HF_2 added to the microemulsion equals the volume of the aqueous solution of YCl_3 initially present. [c] $[NH_4HF_2(aq)] = [YCl_3(aq)]$ [d] Sample prepared at 8 °C, all others at room temperature. [e] 2 mmol/L $ScCl_3$ was added to the initial aqueous solution to obtain YF_3:Sc 5% doped nanoparticles.

A separate batch of 83 nm $(H_3O)Y_3F_{10} \bullet xH_2O$ NPs were synthesized in order to study the effects of sample hydration on ^{89}Y NMR spectra; these SSNMR experiments were performed after experiments on all of the other NP particles had been conducted, as earlier samples (*i.e.*, 21, 37, 49, 67 and 132 nm NPs) were not present in sufficient quantities for continued NMR experimentation. Experimental parameters related to the synthesis of these 83 nm NPs are listed in Table 1. The 83 nm NPs do not appear in any portions of this work aside from ^{19}F- ^{89}Y NMR experiments.

TEM images and electron diffraction patterns were recorded with a JEOL JEM-1230 at an accelerating voltage of 120 kV. Samples were prepared by allowing a drop of the $(H_3O)Y_3F_{10} \bullet xH_2O$ suspensions, as obtained by the syntheses described above, to dry directly on a carbon coated nickel microscope grid, leaving a significant amount of octahedrally-shaped $(H_3O)Y_3F_{10} \bullet xH_2O$ nanoparticles[20] for observations. Size measurements were made on randomly selected particles with

the Scion Image software. Since TEM provides two-dimensional projections, these octahedral nanoparticles appear as hexagons, squares, or rhombuses, depending on their orientation on the TEM grid. Particle size was not measured from two opposite corners of the observed hexagons because these two points are not in the same plane and the length measured would therefore be inaccurate. Instead, the measurements were made between two adjacent corners which correspond to an actual octahedron edge. The octahedral particle sizes reported in this paper refer to length of the octahedron edge. Figure 1 shows TEM images of the $(H_3O)Y_3F_{10} \bullet xH_2O$ NPs. All samples in this study feature a single population of monodisperse NPs, except for the 21 and 132 nm sample, for which small numbers of spherical amorphous particles and triangular prism particles are also observed via TEM. No synthetic conditions were found that allowed for the complete elimination of these secondary particle populations.

Powder X-ray diffraction. Powder XRD (pXRD) experiments were performed on a Bruker AXS HI-STAR system using a General Area Detector Diffractions system with a Cu K_α ($\lambda = 1.54056$ Å) radiation source. Simulations of pXRD patterns from known crystal structures[65] were performed using PowderCell.[66] Rietveld refinements[67] of the 67 nm diameter NPs were completed using the Fullprof suite of programs.[68,69] **Refinements were conducted for 47 variables, including 34 background coefficients fitted using a linear interpolation function, detector zero point (0.06704), lattice parameters and profile coefficients fitted using a Thomson-Cox-Hastings function.[70] However, due to the abundance of light atoms within the proposed structural model and the quality of the pXRD data it was not appropriate to refine the individual atomic thermal parameters of the system. Further information on the refinement parameters is provided in Appendix A of the Supporting**

Information. The structures shown in Figure 4 were generated using the parameters obtained from Rietveld refinement of the pXRD data and the Vesta[71] software program.

Solid-State NMR. Solid-state NMR spectra were collected on a Varian Infinity Plus NMR spectrometer with an Oxford 9.4 T ($\nu_0(^1H)$ = 399.73 MHz) wide-bore magnet with $\nu_0(^{19}F)$ = 376.73 MHz and $\nu_0(^{89}Y)$ = 19.69 MHz. ^1H and ^{19}F magic-angle spinning (MAS) experiments were performed using a Varian/Chemagnetics 2.5 mm HX probe. All ^{89}Y experiments, both static (non-spinning) and MAS, were conducted using a Varian/Chemagnetics 4 mm HXY probe. A Chemagnetics low-γ tuning box and preamplifier were used on the X channel for all ^{89}Y NMR experiments. All samples were packed into 2.5 mm or 4 mm o.d. zirconia rotors. ^1H chemical shifts were referenced to tetramethylsilane (TMS, δ_{iso} = 0.0 ppm) using adamantane (δ_{iso} = 1.85 ppm) as a secondary reference. ^{19}F chemical shifts were referenced with respect to neat $CFCl_3$ (l) (δ_{iso} = 0.0 ppm) using Teflon ($(C_2F_4)_n$, δ_{iso} = -122.0 ppm) as a secondary reference. ^{89}Y chemical shifts were referenced to a 1.0 M YCl_3 (aq) solution (δ_{iso} = 0.0 ppm). ^{45}Sc experiments were attempted; however, the spectra were found to be uninformative, and are not discussed further in this work.

^1H NMR spectra were acquired at a spinning speed of 25 kHz using a standard Bloch decay pulse sequence, with a $\pi/2$ pulse width of 3.0 μs, spectral width of 100 kHz and recycle delay of 5 s. The spectrum of an empty rotor containing Teflon tape (used to fill the space between the cap and the sample) was used to correct experimental spectra for background signal, of which there was little (Figure S2). See Table S1 of the Supporting Information for additional ^1H experimental parameters. ^{19}F MAS NMR spectra were acquired at a spinning speed of 25 kHz under rotor-synchronized conditions using a standard Hahn-echo experiment of the form $(\pi/2)_x$ - τ_1 - $(\pi)_y$ - τ_2 - acq, where τ_1 and

τ_2 represent interpulse delays of 40 and 10 μs, respectively. A ^{19}F $\pi/2$ pulse width of 2.1 μs and spectral width of 400 kHz were used, along with pulse delays of 5 s and 30 s to ensure complete longitudinal (T_1) relaxation of ^{19}F nuclei. Generally, at least two different spinning speeds were employed for all experiments to distinguish isotropic chemical shifts from spinning sidebands; however, only spectra with a spinning speed of 25 kHz were used for analysis due to enhanced signal and resolution of isotropic chemical shifts. See Table S2 for full listings of ^{19}F NMR experimental parameters.

^{19}F-^{89}Y cross polarization[72] (CP) NMR experiments were performed using the VACP pulse sequence[73,74] with two-pulse phase-modulation (TPPM) ^{19}F decoupling.[75] For these experiments, ^{19}F $\pi/2$ pulse widths of 2.5 μs were applied, with contact times from 5 to 11 ms and recycle delays of 5.0 s. Spectral widths of 40 kHz were generally used. Hartmann-Hahn matching fields of 22 kHz for ^{19}F and 43 kHz for ^{89}Y were used in all instances. Experiments were either conducted on static samples, or at a spinning speed of 5 kHz. A ^{19}F decoupling field of 48 kHz was employed in all experiments. For complete experimental details, refer to Table S3.

Simulations of all static solid-state NMR spectra were performed using the WSOLIDS software package.[76] In all cases, uncertainties in the extracted NMR tensor parameters were estimated using bidirectional variation within the simulation software. The uncertainties associated with individual chemical shift tensor components (δ_{11}, δ_{22} and δ_{33}) were calculated through propagation of error from experimental δ_{iso}, Ω and κ values. Processing, line-fitting, and integration of spectra was performed using the NUTS software package from Acorn NMR.

Results and Discussion

Powder X-ray diffraction. pXRD experiments were completed for NPs with diameters of 132, 67, and 37 nm, respectively. Bulk YF_3 belongs to space group *Pnma*; however, our pXRD data (Figure 2) indicate that the NPs crystallize in a different space group. This was also reported in a study by Lemyre *et al*., in which it was found that NPs with different diameter sizes exhibited identical electron diffraction patterns that could not be indexed to the same orthorhombic symmetry as bulk YF_3.[20]

The pXRD data for NPs with diameters of 132, 67, and 37 nm were indexed to a cubic symmetry, in space group *Fd*-3*m*, with a lattice parameter, *a*, of ca. 15.5 Å. Search-match software analysis indicates that these materials adopt a diamond-like structure similar to those previously reported for $(H_3O)Ln_3F_{10} \bullet xH_2O$, where Ln = Lu, Yb, Tm, Er or Y,[77,78] and $(C_3N_2H_{12})_{0.5}Y_3F_{10}$.[79] The Rietveld refinement completed for the 67 nm diameter NPs displays excellent agreement with the calculated model (wR_p = 3.99 % and χ^2 = 1.14, Figure 3) and is consistent with previous reports.[77-80] Full refinement details are given in Tables 2 and 3.

Table 2. Structural parameters for the 67 nm $(H_3O)Y_3F_{10} \bullet 0.6H_2O$ nanoparticles.[a] Space group *Fd*-3*m*, *a* = 15.4876(9) Å and *V* = 3715.0(4) Å^3. $\chi^2 = 1.14$, $wR_p = 3.99$ % and $R_p = 6.23$ %.

Atom	Site	x	y	z	Fractional Occupancy
Y	48f	0.375(2)	0.375(2)	0.0520(3)	1
F1'[b]	96h	0	0.8641(8)	0.5	1
F1'	96h	0	0.1359(8)	0.5	1
F2'	32	0.219(1)	0.219(1)	0.219(1)	1
F3'	32	0.048(1)	0.048(1)	0.048(1)	1
H_3O^+	16d	0.5	0.5	0.5	1
H_2O	48f	0.375(2)	0.375(2)	0.321(4)	0.21(2)

[a] Refinement of our partially hydrated sample yielded $x = 0.6$ with respect to the structural formula $(H_3O)Y_3F_{10} \bullet xH_2O$, and is discussed in the text. [b] Fluorine labels are listed in italics with prime symbols to differentiate these atoms from those within bulk YF_3. See text for details.

Table 3. Relevant interatomic lengths obtained from Rietveld refinement of the 67 nm diameter $(H_3O)Y_3F_{10} \bullet 0.6H_2O$ nanoparticle pXRD pattern.

Bond	Bond Length (Å)
Y - *F1*'	2.337(8)
Y - *F2*'	2.42(2)
Y - *F3*'	2.29(2)
F1' - O	2.49(4)

The diamond-like structure exhibited by these materials (Figure 4) has been described extensively in the literature.[77,79,80] The yttrium ions are in eight-coordinate square antiprismatic polyhedral sites that are face shared around a distorted cubic cavity to form a larger octahedral-like $[Y_6F_{32}]^{14-}$ building block, which is termed a unit of octahedral antiprisms (UOA). Edge- and corner-shared UOA are linked to form a three-dimensional cage-like structure, which allows for

movement of H_2O molecules within cavities linked by channels. In all previous models, the inclusion of charge-balancing ions are reported. It is therefore likely that hydronium ions, as well as water molecules, are located within the void spaces of the structure. This is consistent with the model proposed for $(H_3O)Y_3F_{10} \bullet xH_2O$ in which cavities and channels are statistically populated by zeolithic water molecules, while the hexagonal-shaped cavity entry points within channels are occupied by H_3O^+.[77,78] Rietveld refinements were improved by including the O ions of H_2O and H_3O^+ species, which yielded a general formula of $(H_3O)Y_3F_{10} \bullet 0.6H_2O$. Since the sample for pXRD was dried in an oven prior to analysis in order to drive off zeolithic H_2O, a value of $x = 0.6$ was determined, rather than the expected value of $x = 1$ for a fully hydrated sample.[78] Attempts to replace the hydronium ions with ammonium ions did not improve the refinement, indicating that no residual NH_4^+ from the NH_4HF_2 solvent used during the synthesis remains in the channels. The possibility of F vacancies and/or Cl substitution (from the starting reagent YCl_3) within the $(H_3O)Y_3F_{10} \bullet 0.6H_2O$ framework cannot be discounted, although Cl substitution seems unlikely given that previous work has indicated no presence of Cl whatsoever in samples prepared via the same synthetic route.[20] Rietveld refinements accounting for F vacancies were attempted, but were unsuccessful.

^{1}H MAS NMR Experiments. ^{1}H NMR experiments were performed to ascertain the purity of $(H_3O)Y_3F_{10} \bullet xH_2O$ NPs, as well as to investigate their uptake of water. Spectra of hydrated samples were acquired after exposure to ambient conditions for over two weeks. Previous thermogravimetric analyses and X-ray thermodiffractometry studies indicate that sample decomposition to YF_3 is possible at high temperatures;[77-79] hence, to ensure partial dehydration of zeolithic H_2O without decomposition of the sample or phase changes, only samples that were placed in an oven at 125 °C for at least four hours were subjected to NMR experimentation.

The ^{1}H MAS NMR spectra of fully and partially hydrated 67 nm $(H_3O)Y_3F_{10} \bullet xH_2O$ NPs are shown in Figure 5, and information regarding individual resonances is given in Table S4. The relatively efficient longitudinal ^{1}H relaxation allowed for fairly short pulse delays of 5 s to be employed (Figure S3). Two broad patterns are present between 4 and 7 ppm. The resonances centered at ca. 4.3 and 4.7 ppm in the spectra of the partially and fully hydrated NPs, respectively, correspond to zeolithic water; similar resonances have been observed in ^{1}H NMR spectra of silica-, titania-, and alumina-based mesoporous solids.[81-84] Resonances of comparable breadths are centered at ca. 6.8 ppm for both partially and fully hydrated samples, and correspond to the H_3O^+ species within the NP channels. The integrated area of the H_2O resonance compared to that of H_3O^+ is 14.2 : 10.0 in the fully hydrated sample, but only 7.5 : 10.0 in the partially hydrated sample (Figures S4 and S5, Table S4), indicating that heating at temperatures of 125 °C is sufficient to at least partially eliminate zeolithic water. It should be noted that the integrated area of the H_2O resonance with respect to the H_3O^+ resonance in the spectra of the fully hydrated NPs exceeds the 1:1 stoichiometry expected from a fully hydrated sample,[77,78] which indicates either that additional H_2O must be present in the sample, likely on the surfaces of the NPs, and/or the overlap of H_2O and H_3O^+ resonances results in some uncertainty of the integrated areas.

The sharp resonances observed at 1.4 and 1.0 ppm in both spectra are due to the presence of residual sodium bis(2-ethylhexyl)sulfosuccinate (AOT) and polyoxyethylene(5)nonylphenylether (Igepal520) surfactants, respectively.[85-87] The differences in intensity of the resonances at 1.4 ppm between samples might be linked with the degree of sample hydration, but are likely related in part to the differences in integrated areas of the broad, overlapping adjacent H_2O resonance. The surfactants are likely present in tiny amounts, as suggested by the small integrated areas of their

resonances compared to those of H_2O and H_3O^+ (Table S4). Experiments employing shorter ^1H pulse delays also suggest relatively small amounts of surfactant are present (Figure S3). The surfactant is located on the exterior surface of the NP and is unlikely to occupy channels or cavities due to steric restrictions.[79] ^1H-^{13}C CP NMR experiments detect trace amounts of residual surfactant, consistent with the relatively small amounts indicated by the ^1H MAS spectra. The only ^1H-^{13}C VACP/MAS spectrum that was obtained required an optimized contact time of 3 ms and has two broad resonances of low intensity centered at 85 and 30 ppm (Figure S6), owing to the small quantities of any surfactant present on the NP surface.

Water mobility is known to be exceptionally high within this family of compounds,[77,78] and the sharp resonances at ca. 0.1 ppm in Figure 5 are due to water molecules occupying the void space between $(H_3O)Y_3F_{10} \bullet xH_2O$ NPs. This resonance is more intense in the spectra of fully hydrated NPs and exhibits a chemical shift corresponding to that of highly mobile monomeric gaseous water (*i.e.*, isolated water molecules not interacting with surroundings).[88,89] It is possible that a resonance with this chemical shift could arise from surface hydroxyl species bound to metals[83,90,91] (in this case yttrium); however, this is unlikely, since the ^1H linewidths are too narrow to correspond to surface-bound groups, the NP crystal structure indicates exterior surfaces should largely consist of fluorine, and any surface hydroxyl species would have to arise from uncommon defect sites. Our Rietveld refinements (*vide supra*) and ^{19}F MAS NMR experiments (*vide infra*) also indicate no significant level of F vacancies or substitutions in the $(H_3O)Y_3F_{10} \bullet xH_2O$ NPs. ^1H MAS NMR experiments confirm the purity (*i.e.*, only the expected surface species and water molecules are present) and zeolithic structure of the NPs, but cannot provide any further information on their

molecular-level structure and composition. In order to investigate the structure within the inorganic NP cores, ^{19}F and ^{89}Y SSNMR experiments must be considered.

^{19}F MAS NMR Experiments. The crystal structure of bulk YF_3, which has a space group of *Pnma*, indicates that there is a unique yttrium site which is coordinated by nine fluorine atoms (Figure 6). There are two crystallographically distinct fluorines, **F1** and **F2**, which exist in a ratio of 1:2. The ^{19}F MAS NMR spectrum of bulk YF_3 reveals two sharp resonances with distinct chemical shifts and relative integrated intensities of 2:1 (Figure 7(a)); hence, peaks at -56 and -67 ppm are assigned to **F2** and **F1**, respectively. Both resonances are also associated with spinning sideband manifolds, which under conditions of fast MAS, may be utilized to extract information on the fluorine CS tensors (*vide infra*).

^{19}F MAS NMR experiments were also performed on $(H_3O)Y_3F_{10} \bullet xH_2O$ NPs of varying diameter (Figure 7(b)-(f)). All spectra are of fully hydrated samples unless otherwise stated, due to the much shorter ^{19}F T_1 relaxation times arising from rapidly modulated ^{19}F-^{1}H dipolar couplings involving mobile H_2O molecules (*vide infra*), and correspondingly shorter experimental times. It is apparent that the spectra of the NPs, regardless of size, are clearly distinct from the bulk material in terms of the number of peaks, their relative intensities, and their isotropic chemical shifts. All NP samples have three distinct resonances (δ_{iso} = -45 to -51 ppm, designated "**A**", δ_{iso} = -62 ppm, "**B**", and δ_{iso} = -85 ppm, "**C**"), none of which correspond to the shifts in the spectrum of bulk YF_3. The crystal structure of $(H_3O)Y_3F_{10} \bullet xH_2O$ (Table 2) has three unique fluorine sites *F1′*, *F2′*, and *F3′* (which we italicize and use prime symbols to differentiate from **F1** and **F2** in bulk YF_3), with relative populations of 3:1:1, respectively (Figure 4). Integration in all of the ^{19}F MAS NMR spectra of the NPs (Table 4) reveals a general ratio of 3:1:1 is apparent (including the intensities of both the

isotropic centerbands and the spinning sidebands), although this ratio varies somewhat with NP size (in particular, for the 21 and 132 nm NPs, see below for further discussion). From this ratio, Peak **A** should correspond to site *F1′*, and peaks **B** and **C** to *F2′/F3′*. The assignment of **B** and **C** is ambiguous because *F2′* and *F3′* reside in crystallographically similar sites and cannot be identified via ^{19}F NMR without a priori knowledge of ^{19}F chemical shift assignments. Unfortunately, due to the immense size of the $(H_3O)Y_3F_{10} \bullet xH_2O$ unit cell, first principles calculations using periodic boundary conditions were unable to aid in these chemical shift assignments.

Table 4. Relative integrated areas (including spinning sidebands) of resonances in ^{19}F MAS NMR spectra of hydrated $(H_3O)Y_3F_{10} \bullet xH_2O$ nanoparticles and bulk YF_3. A, B, C, F1, and F2 refer to resonance labels, from high to low frequency (see Figure 7).

Size (nm)	Pulse delay (s)	Integrated Area (A:B:C)	Normalized Area (A:B:C)[a]
21	5	20.9 : 10.5 : 5.6	**2.0 : 1.0 : 0.5**
37	30	28.4 : 11.2 : 7.7	**2.5 : 1.0 : 0.7**
	5	31.2 : 11.4 : 7.9	**2.8 : 1.0 : 0.7**
49 (doped)	30	33.9 : 11.3 : 10.5	**3.0 : 1.0 : 0.9**
	5	39.4 : 11.9 : 10.4	**3.3 : 1.0 : 0.9**
67	30	35.8 : 11.0 : 9.2	**3.2 : 1.0 : 0.8**
	5	31.2 : 11.2 : 9.5	**2.9 : 1.0 : 0.9**
132	30	17.0 : 11.8 : 5.6	**1.4 : 1.0 : 0.5**
	5	18.4 : 11.3 : 6.0	**1.6 : 1.0 : 0.5**
		Integrated Area (F1:F2)	**Normalized Ratio (F1:F2)**
Bulk YF_3	5	4.9 : 10.0	**1.0 : 2.0**

[a] Numbers are normalized to the central resonance **B** and rounded to the first decimal place.

The assignment of resonances in ^{19}F MAS spectra of the NPs was verified by considering their zeolithic properties. The 67 nm NP samples were dried in a lab oven at 125 °C and ^{19}F NMR spectra were acquired immediately afterward. The effect of eliminating zeolithic water in the 67 nm $(H_3O)Y_3F_{10} \bullet xH_2O$ NP sample is shown in the ^{19}F MAS NMR spectra in Figure 8. In ^{19}F MAS NMR spectra of a fully hydrated sample (stored in air) of 67 nm $(H_3O)Y_3F_{10} \bullet xH_2O$ NPs (Figure 8(a),(b)), the expected 3:1:1 integration of *F1′*:*F2′*:*F3′* fluorine resonances is observed. However, when the sample was stored in a 125 °C oven prior to NMR experiments and packed in an airtight rotor (Figure 8(c)), the integration of *F1′*:*F2′*:*F3′* was found to be 1.7:1:1. This disparity in integrated intensities is believed to be due to the effects of proximate zeolithic H_2O on the $T_1(^{19}F)$ relaxation constants of the *F1′* sites, which form the channels and cavities of $(H_3O)Y_3F_{10} \bullet xH_2O$. The H_2O molecules are wholly or partially mobile, which means that ^{1}H-^{19}F dipolar interactions continually fluctuate, contributing to efficient longitudinal ^{19}F relaxation. This is evident from the nearly identical integrated areas resulting from experiments on hydrated samples using a long (30 s) and short (5 s) pulse delay (Table 4). However, when the presence of H_2O within $(H_3O)Y_3F_{10} \bullet xH_2O$ is reduced via heating, a drastic loss in integrated intensity of the *F1′* peak is observed in NMR experiments using the same 5 s pulse delay (*i.e.*, $T_1(^{19}F)$ relaxation is less efficient). No measurement/estimation of $T_1(^{19}F)$ associated with the *F1′* resonance within partially hydrated/heated $(H_3O)Y_3F_{10} \bullet xH_2O$ samples was attempted due to the very long recycle delays and experimental times required to acquire spectra with reasonable S/N (Figure S7). These findings are consistent with the assignment of peaks from the ^{19}F MAS spectra. There is clearly efficient longitudinal relaxation associated with the *F2′*/*F3′* sites, owing to their environments within the ionic network of the UOA, and closer proximity to sources of fluctuating magnetic fields arising from mobile dipolar spin pairs.

The manifold of spinning sidebands that arises from a particular resonance in an MAS experiment (Figure 9) is important for the integration of individual resonances; but, these sidebands also encode information on the fluorine chemical shift (CS) tensors. Spinning sideband manifolds can be analyzed using the Herzfeld-Berger (HB) method to determine approximate CS tensor parameters,[92] though at high spinning rates, the low number of high intensity spinning sidebands limits this analysis. Of the three ^{19}F resonances associated with $(H_3O)Y_3F_{10} \bullet xH_2O$, **A** has the highest chemical shift anisotropy (CSA) (*i.e.*, highest span (Ω) value, Table 5). In contrast, **B** and **C** have smaller Ω values ranging from 110 to 120 ppm and 90 to 130 ppm, respectively. The values of δ_{iso} and Ω associated with **B** and **C** resemble those originating from sites **F1** and **F2** in bulk YF_3. Skew (κ) values for **B** range from 0.1 to 0.5, which correspond well with the κ value of 0.3 associated with site **F2** in bulk YF_3. However, the absence of spinning sidebands (due to a small CSA) associated with both resonance **C** in the NP samples and **F1** in the bulk sample makes it difficult to compare their κ values. The similarity of the isotropic chemical shifts and spans of resonances **B** and **C** (*F2'/F3'*) in $(H_3O)Y_3F_{10} \bullet xH_2O$ NPs to those of **F2** and **F1** in bulk YF_3 suggest that their chemical environments may also be similar.

The **A** resonances have numerous spinning sidebands, which are analyzed to yield CS tensor parameters (Ω = 180 to 200 ppm, κ = 0.6 to 0.9) which are unique from those of **B**, **C**, **F1**, and **F2**. This strongly indicates that the structural environment of the **A** fluorines within the $(H_3O)Y_3F_{10} \bullet xH_2O$ NPs is distinct from the known environments of the bulk YF_3 phase. It has been suggested that H-O-H···F hydrogen bonding is present in systems similar to $(H_3O)Y_3F_{10} \bullet xH_2O$.[77] *F1'*-O distances in our refined crystal structure are 2.5 Å, within the hydrogen bonding range in metal fluoride hydrates,[93] which may partially account for the unique CS tensor parameters associated with

A. A correlation also exists between the δ_{iso} (**A**) and $(H_3O)Y_3F_{10} \bullet xH_2O$ NP size: as the NP size decreases, the chemical shift varies from -51 ppm to -45 ppm (Figure 10). It is notable that δ_{iso} (**A**) does not change with hydration level of the NPs (*vide supra*).

Table 5. ^{19}F chemical shift tensor parameters extracted from MAS spectra of hydrated $(H_3O)Y_3F_{10} \bullet xH_2O$ nanoparticles and bulk YF_3 via Herzfeld-Berger analysis of spinning sidebands.

			Individual CS Tensor Components[c]				
NP Size (nm)	**Peak Label[a]**	**δ_{iso} (ppm)[b]**	**δ_{11} (ppm)**	**δ_{22} (ppm)**	**δ_{33} (ppm)**	**Ω (ppm)[d]**	**κ [e]**
21	A	-51(2)	19(15)	-8(19)	-161(21)	180(30)	0.7(3)
	B	-62(2)	-10(19)	-46(17)	-130(24)	120(40)	0.4(4)
	C	-85(2)	-41(17)	-53(19)	-161(27)	120(40)	0.8(4)
37	A	-49(2)	31(16)	-9(21)	-169(21)	200(30)	0.6(3)
	B	-62(2)	-9(21)	-58(15)	-118(22)	110(40)	0.1(4)
	C	-86(2)	-56(18)	-56(28)	-146(29)	90(40)	1.0(8)[f]
49	A	-49(2)	14(19)	5(27)	-166(29)	180(40)	0.9(4)
	B	-61(2)	-11(19)	41(17)	-131(25)	120(40)	0.5(4)
	C	-85(2)	-31(19)	-63(19)	-160(25)	130(40)	0.5(4)
67	A	-47(2)	26(15)	6(22)	-173(22)	200(30)	0.8(3)
	B	-62(2)	-10(19)	-46(17)	-130(24)	120(40)	0.4(4)
	C	-85(2)	-25(29)	-115(25)	-115(17)	90(40)	-1.0(7)[f]
132	A	-45(2)	28(18)	0(20)	-162(27)	190(40)	0.7(3)
	B	-61(2)	-3(21)	-57(16)	-123(22)	120(40)	0.1(4)
	C	-84(2)	-38(18)	-66(16)	-148(25)	110(40)	0.5(4)
Bulk	F2	-56(2)	-2(15)	-44(13)	-122(18)	120(30)	0.3(3)
	F1	-67(2)	20(31)	-110(33)	-110(20)	130(40)	-1.0(7)[f]

[a] See Figure 7 for labelled spectra. [b] Isotropic chemical shift: $\delta_{iso} = (\delta_{11} + \delta_{22} + \delta_{33})/3$.
[c] Individual CS tensor components and associated uncertainties calculated from experimentally measured δ_{iso}, Ω, and κ values. [d] Span: $\Omega = \delta_{11} - \delta_{33}$. [e] Skew: $\kappa = 3(\delta_{22} - \delta_{iso})/\Omega$. [f] κ value associated with a high uncertainty due to lack of spinning sidebands.

The crystal structure of $(H_3O)Y_3F_{10} \bullet xH_2O$ (Table 2) has three unique fluorine sites in a ratio of 3:1:1, this ratio correlates well with the ratios of the integrated intensities from the ^{19}F MAS NMR spectra of the 37, 49, and 67 nm NPs (Table 4). The synthesis of the $(H_3O)Y_3F_{10} \bullet xH_2O$ NPs is closely related to the synthesis of amorphous YF_3 NPs;[20] it follows that any presence of this amorphous YF_3 phase as an impurity within the NP samples will affect the ^{19}F NMR spectrum. Specifically, since the amorphous YF_3 phase exhibits a similar chemical shift to **B**, the presence of YF_3 may influence the integrated intensity of the **B** resonance in $(H_3O)Y_3F_{10} \bullet xH_2O$ NP spectra, as both ^{19}F NMR resonances arising from crystalline bulk YF_3 (**F1** and **F2**) are proximate to this resonance. Indeed, the integration ratios of the ^{19}F MAS NMR spectra for the 21 nm NPs (2.0 : 1.0 : 0.5) and 132 nm NPs (1.6 : 1.0 : 0.5) are distinct from the predicted 3 : 1 : 1 ratio due to broad patterns underlying the **B** resonance, hinting at the presence of YF_3 in these samples. It is notable that this apparent YF_3 impurity is detectable via SSNMR experiments but not pXRD experiments, indicating that this impurity is amorphous. In order to further investigate the structure of the NPs and the nature of the impurity, ^{19}F-^{89}Y VACP/MAS experiments were performed.

^{19}F-^{89}Y VACP/MAS NMR experiments. ^{89}Y is a low-γ nucleus, and in most inorganic compounds is associated with large $T_1(^{89}Y)$ values (*i.e.*, inefficient longitudinal relaxation), which can lead to long experimental times.[64] Accordingly, ^{19}F-^{89}Y VACP/MAS experiments were employed to exploit the potentially large polarization transfer from ^{19}F to ^{89}Y, as well as the shorter $T_1(^{19}F)$.[72,94] The ^{19}F-^{89}Y VACP/MAS spectrum of bulk YF_3 is shown in Figure 11(a). As expected from the crystal structure (Figure 6), there is a sole resonance corresponding to a single crystallographically unique nine-coordinate yttrium site.

The ^{19}F-^{89}Y VACP/MAS spectra of hydrated $(H_3O)Y_3F_{10} \bullet xH_2O$ NPs (Figure 11) are clearly distinct from the bulk material. The crystal structure of $(H_3O)Y_3F_{10} \bullet xH_2O$ indicates a single Y site and therefore a sole ^{89}Y resonance, but there are two ^{89}Y resonances visible in the NP spectra: one of high intensity at ca. δ_{iso}= -55 ppm (denoted "**X**" for discussion, Figure 11) and a resonance of low, but also NP size-dependent, intensity at δ_{iso} = -36 ppm (denoted "**W**"). The integrated area of **W** is strongly linked to NP size: as the NP size decreases, the relative area of **W** in comparison to **X** increases (Table 6, Figure 12). The relationship between NP size and ^{89}Y NMR integrated area ratio follows a similar exponential trend as the ratio of octahedron surface area to volume, leading to the preliminary interpretation that **W** may correspond to a Y position on or near the NP surface, while **X** may be associated with a Y position deeper in the NP core. The only exception are the 49 nm Sc-doped NPs, where the 5 mol % Sc doping seems to affect the overall structure enough that ^{89}Y chemical shifts are distinct from the other samples.

Table 6. Relative integrated areas (including spinning sidebands) of resonances in ^{19}F-^{89}Y VACP/MAS NMR spectra of hydrated $(H_3O)Y_3F_{10} \bullet xH_2O$ nanoparticles. [a] See Figures 11, 12.

Nanoparticle Size (nm)	δ_{iso} (ppm)	Relative Integrated Area	Peak Integration Ratio [b]	
			Experimental	*Octahedron* [c]
21	-36(2)	4.37(24)	0.437	0.35
	-54(2)	10		
37	-38(2)	2.62(16)	0.262	0.199
	-55(2)	10		
67	-36(2)	1.29(9)	0.129	0.11
	-58(2)	10		
132	-36(2)	0.78(18)	0.078	0.06
	-56(2)	10		
49 [d]	-36(2)	3.37(28)	0.337	0.15
	-56(2)	10		
83 [e]	-23(3)	0.65(15)	0.065	0.089
	-54(3)	10		

[a] Bulk YF_3 only has one ^{89}Y resonance, thus integration not applicable to this sample. [b] Refers to the ratio of the area of the "surface-like" ^{89}Y resonance at ca. -36 ppm versus that of "core-like" ^{89}Y at ca. -55 ppm. [c] Refers to the ratio of surface area to total volume of an ideal octahedron of specified NP edge length, using the formulae $A = 2(\sqrt{3})x^2$ and $V = 1/3(\sqrt{2})x^3$. [d] Since this sample has a major structural change (the presence of Sc, likely in Y sites), its peak integration ratio results in an outlying value. [e] The 83 nm samples were synthesized at a separate point in time, using a similar procedure as for all other NPs. See Experimental section.

Neither of the two major resonances in the spectra of the $(H_3O)Y_3F_{10} \bullet xH_2O$ NPs correspond to bulk YF_3; however, there is a broad, low-intensity peak at ca. δ_{iso} = -105 to -110 ppm, which is most prominent in the spectra of the 21 and 132 nm $(H_3O)Y_3F_{10} \bullet xH_2O$ NP samples, less intense in the spectrum of the 49 nm NPs, and barely visible in the spectra of the 37 and 67 nm samples, consistent with earlier conclusions regarding the presence of an amorphous YF_3 impurity as

suggested by variation in the integrated intensities of ^{19}F MAS NMR resonances. TEM experiments indicate that all samples are composed primarily of monodisperse crystalline NPs, with trace populations of spherical amorphous NPs (see Experimental section),[20] and SSNMR reveals a broad resonance corresponding to bulk YF_3 impurity for some of the samples; hence, the spherical amorphous NPs are likely composed of amorphous YF_3. A less likely possibility also exists that a small fraction of the crystalline NPs may be fully or partially composed of crystalline bulk YF_3, although evidence of this was not observed in our experiments. Further, from the synthetic procedure and parameters given in the Experimental section (*vide supra*), it appears as if the use of AOT surfactant in NP synthesis suppresses the formation of YF_3. Differences in experimental ^{19}F-^{89}Y CP mixing times did not have an effect on the integration or intensities of the individual peaks associated with $(H_3O)Y_3F_{10} \bullet xH_2O$ (Figure S8).

A separate batch of 83 nm $(H_3O)Y_3F_{10} \bullet xH_2O$ NPs, synthesized in a similar manner (but at a later date), were employed to study the effects of sample hydration on ^{19}F-^{89}Y VACP(/MAS) NMR spectra and to confirm the assignments of the **W** and **X** resonances (see Experimental); these NPs have similar TEM images (Figure S9) and NMR spectra (*vide infra*) to those of the initial batches of $(H_3O)Y_3F_{10} \bullet xH_2O$ NPs. Both resonances **W** and **X** are present in ^{19}F-^{89}Y VACP/MAS NMR spectra of the partially and fully hydrated 83 nm NP samples (Figure 13), although the resolution of the **W** peak in the spectrum of the former is very poor, translating to sizable uncertainty regarding its exact position and breadth (Table 6, Table S5) . The spectrum of the fully hydrated 83 nm NP sample displays higher S/N and much better resolution of the **W** and **X** sites, although both spectra were recorded with similar acquisition parameters. Y sites in the partially dehydrated sample may be strongly, weakly, or not coordinated to surface H_2O species; hence, the broad and poorly resolved

W peaks in these samples likely arises from (i) a distribution of ^{89}Y chemical shifts and/or (ii) a distribution of $T_2(^{89}Y)$ constants, originating from interactions between surface yttria and water molecules. The hydration-linked changes in these ^{19}F-^{89}Y VACP/MAS NMR spectra confirm that resonance **W** corresponds to a Y position on or near the NP surface, while **X** is linked with a Y position within the NP core

Static ^{19}F-^{89}Y VACP NMR experiments. The sensitivity of ^{19}F-^{89}Y VACP/MAS NMR spectra to surface- and core-like yttrium environments invites examination of the complete ^{89}Y CS tensor parameters. In order to extract anisotropic ^{89}Y CS tensor parameters, static (non-spinning) VACP experiments were performed. The NMR spectra obtained for the NP samples of all sizes are distinct from bulk YF_3 (Figure 14), which exhibits a distinct powder pattern from which CS tensor parameters are readily extracted. All of the hydrated $(H_3O)Y_3F_{10} \bullet xH_2O$ NP samples have spectra which suggest the presence of multiple sites and perhaps some degree of disorder. An impurity, identified as bulk YF_3, makes small contributions to all powder patterns in the region of δ_{iso} = -107 ppm (*vide supra*).

It is possible to simulate the static ^{19}F-^{89}Y VACP powder patterns of the bulk sample and the NPs and extract their respective ^{89}Y CS tensor parameters (Table 7, Figure 15). Bulk YF_3 (Figure 15(a)) yields a well-defined powder pattern which corresponds to CS tensor parameters of Ω = 110(5) ppm and κ = 0.20(5)). Simulations of NP spectra feature two ^{89}Y resonances, with relative integrated intensities and δ_{iso} closely resembling those obtained from the corresponding VACP/MAS experiments. Owing to the lack of distinct features in all of the NP powder patterns, the ^{89}Y CS tensor parameters have a higher degree of uncertainty than those of the bulk sample. The

two ^{89}Y powder patterns evident in spectra of $(H_3O)Y_3F_{10} \bullet xH_2O$ NPs of all sizes correspond to CS tensor parameters of Ω = 50(10) ppm and κ = -0.4(1).

Table 7. ^{89}Y CS tensor parameters extracted from static ^{19}F-^{89}Y VACP NMR experiments on hydrated $(H_3O)Y_3F_{10} \bullet xH_2O$ NPs. [a]

Nanoparticle Size (nm)	δ_{iso} (ppm)	Ω (ppm)	κ	Relative Intensity (%)
21	-36(3)	50(10)	-0.4(1)	42
	-54(3)	50(10)	-0.4(1)	100
37	-38(3)	50(10)	-0.4(1)	26
	-55(3)	50(10)	-0.4(1)	100
49	-36(3)	50(10)	-0.4(1)	35
	-54(4) [b]	50(10)	-0.4(1)	100
67	-36(3)	50(10)	-0.4(1)	13
	-55(4) [b]	50(10)	-0.4(1)	100
132	-36(3)	50(10)	-0.4(1)	20 [c]
	-54(4) [b]	50(10)	-0.4(1)	100
Bulk YF_3	-107(2)	110(5)	0.20(5)	-
83 [d]	-28(3)	50 (10)	-0.4(1)	19
(Fully hydrated)	-55(3) [b]	50 (10)	-0.4(1)	100
83 [d,e]	-28(5)	60(20)	-0.4(2)	18
(Partially hydrated)	-54(4) [b]	60(20)	-0.4(2)	100

[a] All simulations of spectra required ca. 175 Hz of line broadening. [b] δ_{iso} of static simulation differs from VACP/MAS result. [c] Relative intensity of static simulation differs from that of VACP/MAS experiment. [d] Refers to a NP sample prepared separately but in a similar manner, see discussion in text. [e] The fully hydrated sample yields a relatively broad, featureless lineshape, which provides little data about the CS tensor. This is reflected in the associated uncertainty of parameters for this sample.

Static ^{19}F-^{89}Y VACP experiments were also performed on partially and fully hydrated 83 nm $(H_3O)Y_3F_{10} \bullet xH_2O$ NPs (Figure 16, Table 7). The most striking differences between these spectra are the breadths and shapes of the powder patterns. Much like the VACP/MAS spectra, the spectrum of the partially hydrated NPs is broader and the individual patterns are more difficult to resolve in comparison to those of the fully hydrated NPs; this is consistent with the notion that there are larger distributions of chemical shifts and/or $T_2(^{89}Y)$ values associated with the "**W**" powder pattern centered at δ_{iso} = -36 ppm. Fully and partially hydrated samples give rise to two sets of similar ^{89}Y CS parameters which are differentiated by δ_{iso} (Table 7), but share common anisotropic parameters (*i.e.*, Ω and κ).

Conclusions

We have shown, using powder XRD and SSNMR methods, that the intended reverse micelle synthesis of YF_3 NPs yields crystalline NPs of controllable size and shape, with a distinct composition and phase ($(H_3O)Y_3F_{10} \bullet xH_2O$). The zeolithic channels and cavities are populated by hydrogen-bound water molecules. Residual surfactant from the synthesis is limited to the NP surface in relatively small amounts. ^{19}F MAS NMR spectra show a clear difference in phase between bulk YF_3 and the NP samples: three unique resonances are observed for the latter, in accordance with the crystal structure of $(H_3O)Y_3F_{10} \bullet xH_2O$. The integration of these resonances, along with extracted ^{19}F CS tensor parameters, allow for their partial assignment. The ^{19}F nuclei corresponding to the fluorine resonance **A**, which are demonstrated to compose the zeolithic channels and cavities, have longer T_1 relaxation times when H_2O is not present within the sample, owing to the reduction of rapidly modulated ^{19}F-^{1}H dipolar couplings that serve to increase the efficiency of longitudinal

relaxation. ^{19}F-^{89}Y VACP/MAS spectra of $(H_3O)Y_3F_{10} \bullet xH_2O$ NPs exhibit two resonances of dissimilar intensity which do not correspond to bulk YF_3; the less intense resonance has an integrated area directly correlated to NP size and is linked to surface-like yttrium environments. MAS and static ^{19}F-^{89}Y spectra of partially hydrated samples confirm that two ^{89}Y resonances are present. The less intense ^{89}Y resonance associated with surface yttrium species is especially difficult to resolve in the partially hydrated species, since surface Y sites may or may not be interacting with water molecules, leading to a distribution of ^{89}Y chemical shifts and/or $T_2(^{89}Y)$ constants. Static ^{19}F-^{89}Y VACP experiments show that the surface and core yttrium environments associated with these $(H_3O)Y_3F_{10} \bullet xH_2O$ NPs are similar, confirming only small amounts of ligands and surfactant are bound to the NP surface. Finally, with knowledge of the intended product and synthetic precursors, along with the combined use of pXRD and SSNMR, we have demonstrated that it is possible to identify an NP product, probe its macroscopic zeolithic behaviour at the molecular level, link NMR resonances to overall NP size, establish product purity with respect to contaminants, and determine the identity and morphology of the impurities. This experimental protocol offers much promise for the identification, characterization, and future rational design of NPs.

Acknowledgements

BEGL thanks the Ontario Ministry of Training, Colleges, and Universities for a Queen Elizabeth II Ontario Graduate Scholarship in Science and Technology (QEII-GSST). RWS thanks the Natural Sciences and Engineering Research Council (NSERC, Canada), the Canadian Foundation for Innovation, the Ontario Innovation Trust and the University of Windsor for support. RWS also thanks the Ontario Ministry of Research and Innovation for an Early Researcher Award, and

acknowledges the Centre for Catalysis and Materials Research (CCMR) at the University of Windsor for additional funding. JLL, AB, MB, and AMR would like to acknowledge NanoQuébec, le Fonds Québécois de la recherche sur la nature et les technologies (FQRNT) and NSERC for their financial support.

Supporting Information Available: Additional information on Rietveld refinements of pXRD data, complete NMR experimental parameters, additional ^{1}H and ^{19}F-^{89}Y NMR spectrum integrations, supplemental ^{1}H, ^{19}F, ^{19}F-^{89}Y, and ^{1}H-^{13}C NMR spectra, and TEM images of 83 nm nanoparticles. This material is available free of charge *via* the Internet at http://pubs.acs.org.

Figure Captions

Figure 1. TEM images of octahedrally-shaped $(H_3O)Y_3F_{10} \bullet xH_2O$ nanoparticles, with a measured edge length of (a) 21 nm, (b) 37 nm, (c) 49 nm, (d) 67 nm, and (e) 132 nm. Octahedron edges shown in (d) are highlighted to demonstrate NP measurements.

Figure 2. pXRD patterns collected for bulk YF_3 (space group *Pnma*) and $(H_3O)Y_3F_{10} \bullet xH_2O$ nanoparticles, (space group *Fd*-3*m*), with nanoparticle diameters listed in nm. A simulated pXRD pattern for bulk YF_3 is displayed at the bottom.

Figure 3. Rietveld profile for the 67 nm diameter $(H_3O)Y_3F_{10} \bullet xH_2O$ nanoparticles using the space group *Fd*-3*m*.

Figure 4. Schematic representation of the $(H_3O)Y_3F_{10}{\cdot}xH_2O$ diamond-like structure where (a) represents the YF_8 coordination polyhedra, (b) represents the $[Y_6F_{32}]^{14-}$ UOA octahedral-like building units, (c) and (d) represent the cage like structure exhibited by the nanoparticles. Fluorine ions are denoted by blue spheres and the yttrium polyhedra are denoted in grey. In (c) the red spheres denote the oxygen ions associated with the H_3O^+ moiety and in (d) the purple spheres indicate the void spaces. The positions of the water molecules within the cages are not shown.

Figure 5. ^{1}H MAS spectra of 67 nm $(H_3O)Y_3F_{10} \bullet xH_2O$ nanoparticles at a spinning speed of 25 kHz. The red trace corresponds to a fully hydrated (x = 1) sample, and the blue trace corresponds to a partially hydrated (x < 1) sample. Inset left: $(H_3O)Y_3F_{10} \bullet xH_2O$ crystal structure.

Figure 6. (a) The local nine-coordinate environment about yttrium and (b) the extended structure of bulk YF_3. There are two fluorine sites in a 1:2 ratio and one unique yttrium center.

Figure 7. ^{19}F MAS NMR spectra of (a) bulk YF_3 and hydrated $(H_3O)Y_3F_{10} \bullet xH_2O$ nanoparticles of size (b) 132 nm, (c) 67 nm, (d) 49 nm, (e) 37 nm, and (f) 21 nm. Spectra recorded at a spinning speed of 25 kHz. F1 and F2 in (a) denote isotropic chemical shifts in bulk YF_3, A, B, and C for (b)-(f) denote isotropic chemical shifts in $(H_3O)Y_3F_{10} \bullet xH_2O$, while asterisks (*) denote spinning sidebands.

Figure 8. ^{19}F MAS NMR spectra for 67 nm $(H_3O)Y_3F_{10} \bullet xH_2O$ nanoparticles (a) as received (hydrated), (b) after prolonged air exposure (hydrated), (c) after 12 hours of heating at 125 °C

(partially hydrated). Spectra were recorded at a spinning speed of 25 kHz. Peak labels indicate resonance assignment and integration ratios (including spinning sidebands). Asterisks (*) denote spinning sidebands.

Figure 9. Deconvoluted ^{19}F MAS NMR spectra of hydrated 37 nm $(H_3O)Y_3F_{10} \bullet xH_2O$ nanoparticles. Spinning sidebands are labeled according to the corresponding isotropic peak. Spectra were recorded at a spinning speed of 25 kHz.

Figure 10. Change in δ_{iso} of resonance A correlated with nanoparticle size in ^{19}F MAS NMR spectra of hydrated $(H_3O)Y_3F_{10} \bullet xH_2O$ nanoparticles of size (b) 132 nm, (c) 67 nm, (d) 49 nm, (e) 37 nm, and (f) 21 nm. Bulk YF_3 is shown in (a) for comparison. Spectra recorded at a spinning speed of 25 kHz. A, B, and C denote isotropic chemical shifts in hydrated $(H_3O)Y_3F_{10} \bullet xH_2O$.

Figure 11. ^{19}F-^{89}Y VACP/MAS NMR spectra of bulk YF_3 (a) and hydrated $(H_3O)Y_3F_{10} \bullet xH_2O$ nanoparticles of size (b) 132 nm, (c) 67 nm, (d) 49 nm, (e) 37 nm, and (f) 21 nm. Spectra recorded at a spinning speed of 5 kHz. Inset left: The dashed grey line indicates traces of bulk YF_3 exist as various degrees of impurity in the $(H_3O)Y_3F_{10} \bullet xH_2O$ nanoparticle samples.

Figure 12. The graph depicts the relationship between the ratio of the integrated areas of **W** and **X** peaks and $(H_3O)Y_3F_{10} \bullet xH_2O$ NP size in ^{19}F-^{89}Y VACP/MAS spectra of hydrated samples. Blue data points represent experimental ratios, red data points represent surface area/volume ratios of ideal

octahedra (see Table 6). The green outlier represents the 49 nm Sc-doped $(H_3O)Y_3F_{10} \bullet xH_2O$ nanoparticles.

Figure 13. ^{19}F-^{89}Y VACP/MAS NMR spectra of 83 nm $(H_3O)Y_3F_{10} \bullet xH_2O$ nanoparticles, where (a) is a fully hydrated sample, and (b) is only partially hydrated. Spectra were recorded at a spinning speed of 5 kHz.

Figure 14. Static ^{19}F-^{89}Y VACP NMR spectra of (a) bulk YF_3 and hydrated $(H_3O)Y_3F_{10} \bullet xH_2O$ nanoparticles of size (b) 132 nm, (c) 67 nm, (d) 49 nm, (e) 37 nm, and (f) 21 nm.

Figure 15. Static ^{19}F-^{89}Y VACP NMR spectra and simulation of (a) bulk YF_3 and (b) hydrated 37 nm $(H_3O)Y_3F_{10} \bullet xH_2O$ nanoparticles. See Table 7.

Figure 16. Overlaid static ^{19}F-^{89}Y VACP NMR spectra of fully (black) and partially (orange) hydrated 83 nm $(H_3O)Y_3F_{10} \bullet xH_2O$ nanoparticles are shown in (a). Simulations of spectra of the fully ((b), inset left), and partiallly ((c), inset right) hydrated NPs are also shown. See Table 7.

References

(1) Anker, J. N.; Hall, W. P.; Lyandres, O.; Shah, N. C.; Zhao, J.; Van Duyne, R. P. *Nat. Mater.* **2008**, *7*, 442.

(2) Brigger, I.; Dubernet, C.; Couvreur, P. *Adv. Drug Delivery Rev.* **2002**, *54*, 631.

(3) Hutter, E.; Fendler, J. H. *Adv. Mater.* **2004**, *16*, 1685.

(4) Klimov, V. I.; Mikhailovsky, A. A.; Xu, S.; Malko, A.; Hollingsworth, J. A.; Leatherdale, C. A.; Eisler, H. J.; Bawendi, M. G. *Science* **2000**, *290*, 314.

(5) Lal, S.; Link, S.; Halas, N. J. *Nat. Photonics* **2007**, *1*, 641.

(6) Panyam, J.; Labhasetwar, V. *Adv. Drug Delivery Rev.* **2003**, *55*, 329.

(7) Wang, X.; Zhuang, J.; Peng, Q.; Li, Y. D. *Nature* **2005**, *437*, 121.

(8) Wang, X.; Li, Y. D. *Chem. Eur. J.* **2003**, *9*, 5627.

(9) Mai, H. X.; Zhang, Y. W.; Si, R.; Yan, Z. G.; Sun, L. D.; You, L. P.; Yan, C. H. *J. Am. Chem. Soc.* **2006**, *128*, 6426.

(10) Chan, W. C. W.; Maxwell, D. J.; Gao, X. H.; Bailey, R. E.; Han, M. Y.; Nie, S. M. *Curr. Opin. Biotechnol.* **2002**, *13*, 40.

(11) Bunzli, J. C. G. *Acc. Chem. Res.* **2006**, *39*, 53.

(12) Chatteriee, D. K.; Rufalhah, A. J.; Zhang, Y. *Biomaterials* **2008**, *29*, 937.

(13) Boyer, J. C.; Cuccia, L. A.; Capobianco, J. A. *Nano Lett.* **2007**, *7*, 847.

(14) Heer, S.; Lehmann, O.; Haase, M.; Gudel, H. U. *Angew. Chem. Int. Ed.* **2003**, *42*, 3179.

(15) Wang, F.; Han, Y.; Lim, C. S.; Lu, Y. H.; Wang, J.; Xu, J.; Chen, H. Y.; Zhang, C.; Hong, M. H.; Liu, X. G. *Nature* **2010**, *463*, 1061.

(16) Wang, F.; Liu, X. G. *J. Am. Chem. Soc.* **2008**, *130*, 5642.

(17) Wang, F.; Liu, X. G. *Chem. Soc. Rev.* **2009**, *38*, 976.

(18) Tissue, B. M. *Chem. Mat.* **1998**, *10*, 2837.

(19) Stouwdam, J. W.; Hebbink, G. A.; Huskens, J.; van Veggel, F. C. J. M. *Chem. Mat.* **2003**, *15*, 4604.

(20) Lemyre, J. L.; Ritcey, A. M. *Chem. Mat.* **2005**, *17*, 3040.

(21) Lemyre, J. L.; Lamarre, S.; Beaupre, A.; Ritcey, A. M. *Langmuir* **2011**, *27*, 11824.

(22) Fedorov, P. P.; Luginina, A. A.; Kuznetsov, S. V.; Osiko, V. V. *J. Fluorine Chem.* **2011**, *132*, 1012.

(23) Li, C. X.; Lin, J. *J. Mat. Chem.* **2010**, *20*, 6831.

(24) Vetrone, F.; Capobianco, J. A. *Int. J. Nanotechnol.* **2008**, *5*, 1306.

(25) Kuznetsov, S. V.; Osiko, V. V.; Tkatchenko, E. A.; Fedorov, P. P. *Russ. Chem. Rev.* **2006**, *75*, 1065.

(26) Yi, G. S.; Lu, H. C.; Zhao, S. Y.; Yue, G.; Yang, W. J.; Chen, D. P.; Guo, L. H. *Nano Lett.* **2004**, *4*, 2191.

(27) Lu, H. C.; Yi, G. S.; Zhao, S. Y.; Chen, D. P.; Guo, L. H.; Cheng, J. *J. Mat. Chem.* **2004**, *14*, 1336.

(28) Guo, H. C.; Qian, H. S.; Idris, N. M.; Zhang, Y. *Nanomed. Nanotechnol. Biol. Med.* **2010**, *6*, 486.

(29) Rossetti, F. C.; Fantini, M. C. A.; Carollo, A. R. H.; Tedesco, A. C.; Bentley, M. *J. Pharm. Sci.* **2011**, *100*, 2849.

(30) Pelliccia, D.; Nikulin, A. Y.; Muddle, B. C.; Sakata, O. *Scr. Mater.* **2011**, *64*, 613.

(31) Beyerlein, K. R.; Solla-Gullon, J.; Herrero, E.; Garnier, E.; Pailloux, F.; Leoni, M.; Scardi, P.; Snyder, R. L.; Aldaz, A.; Feliu, J. M. *Mater. Sci. Eng., A* **2010**, *528*, 83.

(32) Vogel, W.; He, W.; Huang, Q. H.; Zou, Z. Q.; Zhang, X. G.; Yang, H. *Int. J. Hydrogen Energy* **2010**, *35*, 8609.

(33) Malis, O.; Radu, M.; Mott, D.; Wanjala, B.; Luo, J.; Zhong, C. J. *Nanotechnology* **2009**, *20*, 245708.

(34) Kumpf, C. *Appl. Phys. A* **2006**, *85*, 337.

(35) Yan, W. F.; Petkov, V.; Mahurin, S. M.; Overbury, S. H.; Dai, S. *Catal. Commun.* **2005**, *6*, 404.

(36) Lee, K. M.; Lee, D. J.; Ahn, H. *Mater. Lett.* **2004**, *58*, 3122.

(37) Zhang, P.; Sham, T. K. *Phys. Rev. Lett.* **2003**, *90*, 245502.

(38) Sun, X. C.; Reyes-Gasga, J.; Dong, X. L. *Mol. Phys.* **2002**, *100*, 3147.

(39) Westesen, K.; Siekmann, B.; Koch, M. H. J. *Int. J. Pharm.* **1993**, *93*, 189.

(40) Avadhut, Y. S.; Weber, J.; Hammarberg, E.; Feldmann, C.; Schellenberg, I.; Pottgen, R.; der Gunne, J. S. A. *Chem. Mat.* **2011**, *23*, 1526.

(41) Verkuijlen, M. H. W.; Gao, J. B.; Adelhelm, P.; van Bentum, P. J. N.; de Jongh, P. E.; Kentgens, A. P. M. *J. Phys. Chem. C* **2010**, *114*, 4683.

(42) Grunberg, A.; Xu, Y. P.; Breitzke, H.; Buntkowsky, G. *Chem. Eur. J.* **2010**, *16*, 6993.

(43) Gervais, C.; Smith, M. E.; Pottier, A.; Jolivet, J. P.; Babonneau, F. *Chem. Mat.* **2001**, *13*, 462.

(44) Sreeja, V.; Smitha, T. S.; Nand, D.; Ajithkumar, T. G.; Joy, P. A. *J. Phys. Chem. C* **2008**, *112*, 14737.

(45) Sepelak, V.; Bergmann, I.; Indris, S.; Feldhoff, A.; Hahn, H.; Becker, K. D.; Grey, C. P.; Heitjans, P. *J. Mat. Chem.* **2011**, *21*, 8332.

(46) Alam, T. M. *Mater. Chem. Phys.* **2004**, *85*, 310.

(47) Jager, C.; Welzel, T.; Meyer-Zaika, W.; Epple, M. *Magn. Reson. Chem.* **2006**, *44*, 573.

(48) Avolio, R.; Gentile, G.; Avella, M.; Capitani, D.; Errico, M. E. *J. Polym. Sci., Part A: Polym. Chem.* **2010**, *48*, 5618.

(49) Sepelak, V.; Becker, K. D.; Bergmann, I.; Suzuki, S.; Indris, S.; Feldhoff, A.; Heitjans, P.; Grey, C. P. *Chem. Mat.* **2009**, *21*, 2518.

(50) Berrettini, M. G.; Braun, G.; Hu, J. G.; Strouse, G. F. *J. Am. Chem. Soc.* **2004**, *126*, 7063.

(51) O'Connor, R. D.; Zhang, Q.; Wooley, K. L.; Schaefer, J. *Helv. Chim. Acta* **2002**, *85*, 3219.

(52) Ratcliffe, C. I.; Yu, K.; Ripmeester, J. A.; Zaman, M. B.; Badarau, C.; Singh, S. *Phys. Chem. Chem. Phys.* **2006**, *8*, 3510.

(53) Novio, F.; Philippot, K.; Chaudret, B. *Catal. Lett.* **2010**, *140*, 1.

(54) Mallissery, S. K.; Gudat, D. *Dalton Trans.* **2010**, *39*, 4280.

(55) Fiurasek, P.; Reven, L. *Langmuir* **2007**, *23*, 2857.

(56) Giuliani, J. R.; Harley, S. J.; Carter, R. S.; Power, P. P.; Augustine, M. P. *Solid State Nucl. Magn. Reson.* **2007**, *32*, 1.

(57) de Monredon, S.; Cellot, A.; Ribot, F.; Sanchez, C.; Armelao, L.; Gueneau, L.; Delattre, L. *J. Mat. Chem.* **2002**, *12*, 2396.

(58) Lo, A. Y. H.; Sudarsan, V.; Sivakumar, S.; van Veggel, F.; Schurko, R. W. *J. Am. Chem. Soc.* **2007**, *129*, 4687.

(59) Reyes-Garcia, E. A.; Sun, Y. P.; Reyes-Gil, K.; Raftery, D. *J. Phys. Chem. C* **2007**, *111*, 2738.

(60) Reyes-Garcia, E. A.; Sun, Y. P.; Reyes-Gil, K. R.; Raftery, D. *Solid State Nucl. Magn. Reson.* **2009**, *35*, 74.

(61) Duan, X. L.; Yuan, D. R.; Yu, F. P. *Inorg. Chem.* **2011**, *50*, 5460.

(62) Dolbier, W. R., Ed. *Guide to Fluorine NMR for Organic Chemists*; Wiley: Hoboken, NJ, 2009.

(63) Miller, J. M. *Prog. Nucl. Magn. Reson. Spectrosc.* **1996**, *28*, 255.

(64) MacKenzie, K. J. D.; Smith, M. E. *Multinuclear Solid-State NMR of Inorganic Materials*; Pergamon Press: Oxford, 2002.

(65) Zalkin, A.; Templeton, D. H. *J. Am. Chem. Soc.* **1953**, *75*, 2453.

(66) Kraus, W.; Nolze, G., Powdercell, v. 2.4, Federal Institute for Materials Research and Testing: Berlin, Germany, 2000.

(67) Rietveld, H. *J. Appl. Crystallogr.* **1969**, *2*, 65.

(68) Rodriguez-Carvajal, J. *Physica B* **1993**, *192*, 55.

(69) Rodriguez-Carvajal, J. *J. Commission on Powder Diffraction (IUCr) Newsletter* **2001**, *26*, 12.

(70) Thompson, P.; Cox, D. E.; Hastings, J. B. *J. Appl. Crystallogr.* **1987**, *20*, 79.

(71) Momma, K.; Izumi, F. *J. Appl. Crystallogr.* **2011**, *44*, 1272.

(72) Pines, A.; Gibby, M. G.; Waugh, J. S. *J. Chem. Phys.* **1973**, *59*, 569.

(73) Peersen, O. B.; Wu, X.; Kustanovich, I.; Smith, S. O. *J. Magn. Reson., Ser. A* **1993**, *104*, 334.

(74) Peersen, O. B.; Wu, X.; Smith, S. O. *J. Magn. Reson., Ser. A* **1994**, *106*, 127.

(75) Bennett, A. E.; Rienstra, C. M.; Auger, M.; Lakshmi, K. V.; Griffin, R. G. *J. Chem. Phys.* **1995**, *103*, 6951.

(76) Eichele, K.; Wasylishen, R. E., WSolids1: Solid-State NMR Spectrum Simulation, version 1.17.30, University of Tübingen, Tübingen, Germany, 2001.

(77) Maguer, J. J.; Crosnier-Lopez, M. P.; Courbion, G. *J. Solid State Chem.* **1997**, *128*, 42.

(78) Le Berre, F.; Boucher, E.; Allain, M.; Courbion, G. *J. Mat. Chem.* **2000**, *10*, 2578.

(79) Stephens, N. F.; Lightfoot, P. *J. Solid State Chem.* **2007**, *180*, 260.

(80) Maguer, J. J.; Courbion, G. *J. Solid State Chem.* **1997**, *128*, 52.

(81) Trebosc, J.; Wiench, J. W.; Huh, S.; Lin, V. S. Y.; Pruski, M. *J. Am. Chem. Soc.* **2005**, *127*, 3057.

(82) Grunberg, B.; Emmler, T.; Gedat, E.; Shenderovich, I.; Findenegg, G. H.; Limbach, H. H.; Buntkowsky, G. *Chem. Eur. J.* **2004**, *10*, 5689.

(83) Crocker, M.; Herold, R. H. M.; Wilson, A. E.; Mackay, M.; Emeis, C. A.; Hoogendoorn, A. M. *J. Chem. Soc., Faraday Trans.* **1996**, *92*, 2791.

(84) Hunger, M.; Freude, D.; Pfeifer, H. *J. Chem. Soc., Faraday Trans.* **1991**, *87*, 657.

(85) Sheih, P. S.; Fendler, J. H. *J. Chem. Soc., Faraday Trans. 1* **1977**, *73*, 1480.

(86) Demarco, A.; Menegatti, E.; Luisi, P. L. *J. Biochem. Bioph. Methods* **1986**, *12*, 325.

(87) Law, S. J.; Britton, M. M. *Langmuir* **2012**, *28*, 11699.

(88) Schneider, W. G.; Bernstein, H. J.; Pople, J. A. *J. Chem. Phys.* **1958**, *28*, 601.

(89) Hindman, J. C. *J. Chem. Phys.* **1966**, *44*, 4582.

(90) Lyons, D. M.; McGrath, J. P.; Morris, M. A. *J. Phys. Chem. B* **2003**, *107*, 4607.

(91) Huittinen, N.; Sarv, P.; Lehto, J. *J. Colloid Interface Sci.* **2011**, *361*, 252.

(92) Herzfeld, J.; Berger, A. E. *J. Chem. Phys.* **1980**, *73*, 6021.

(93) Simonov, V. I.; Bukvetsky, B. V. *Acta Crystallogr., Sect. B: Struct. Sci* **1978**, *34*, 355.

(94) Pines, A.; Waugh, J. S.; Gibby, M. G. *Chem. Phys. Lett.* **1972**, *15*, 373.

Table of Contents Graphic

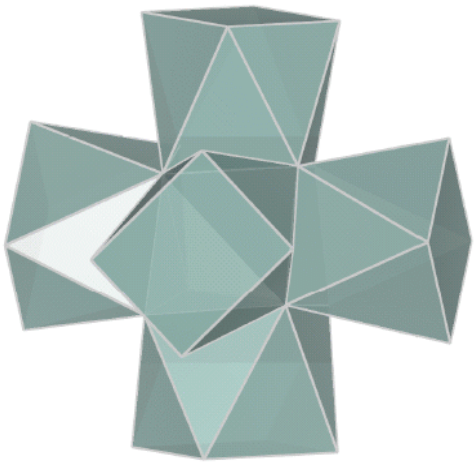

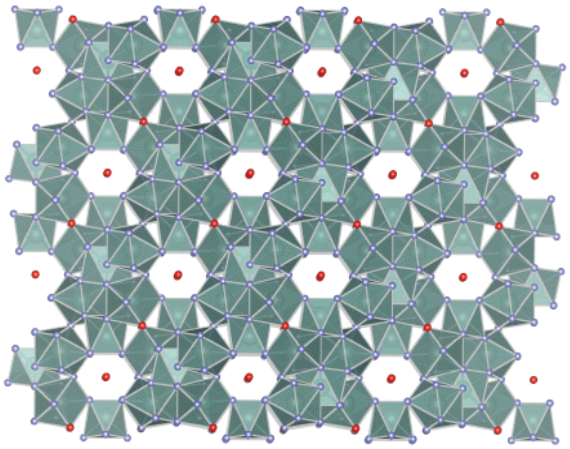

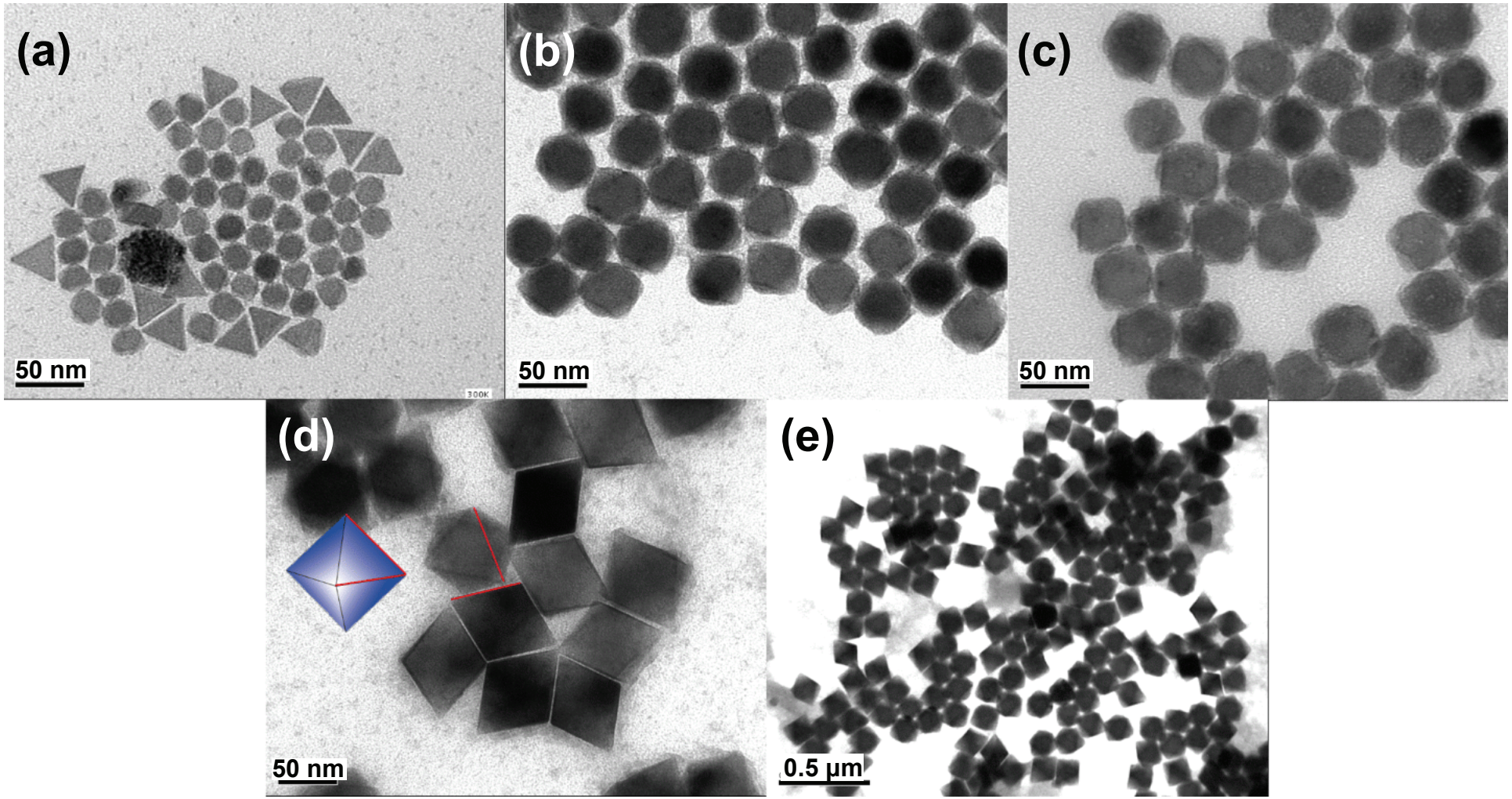

Figure 1. TEM images of octahedrally-shaped $(H_3O)Y_3F_{10} \bullet xH_2O$ nanoparticles, with a measured edge length of (a) 21 nm, (b) 37 nm, (c) 49 nm, (d) 67 nm, and (e) 132 nm. Octahedron edges shown in (d) are highlighted to demonstrate NP measurements.

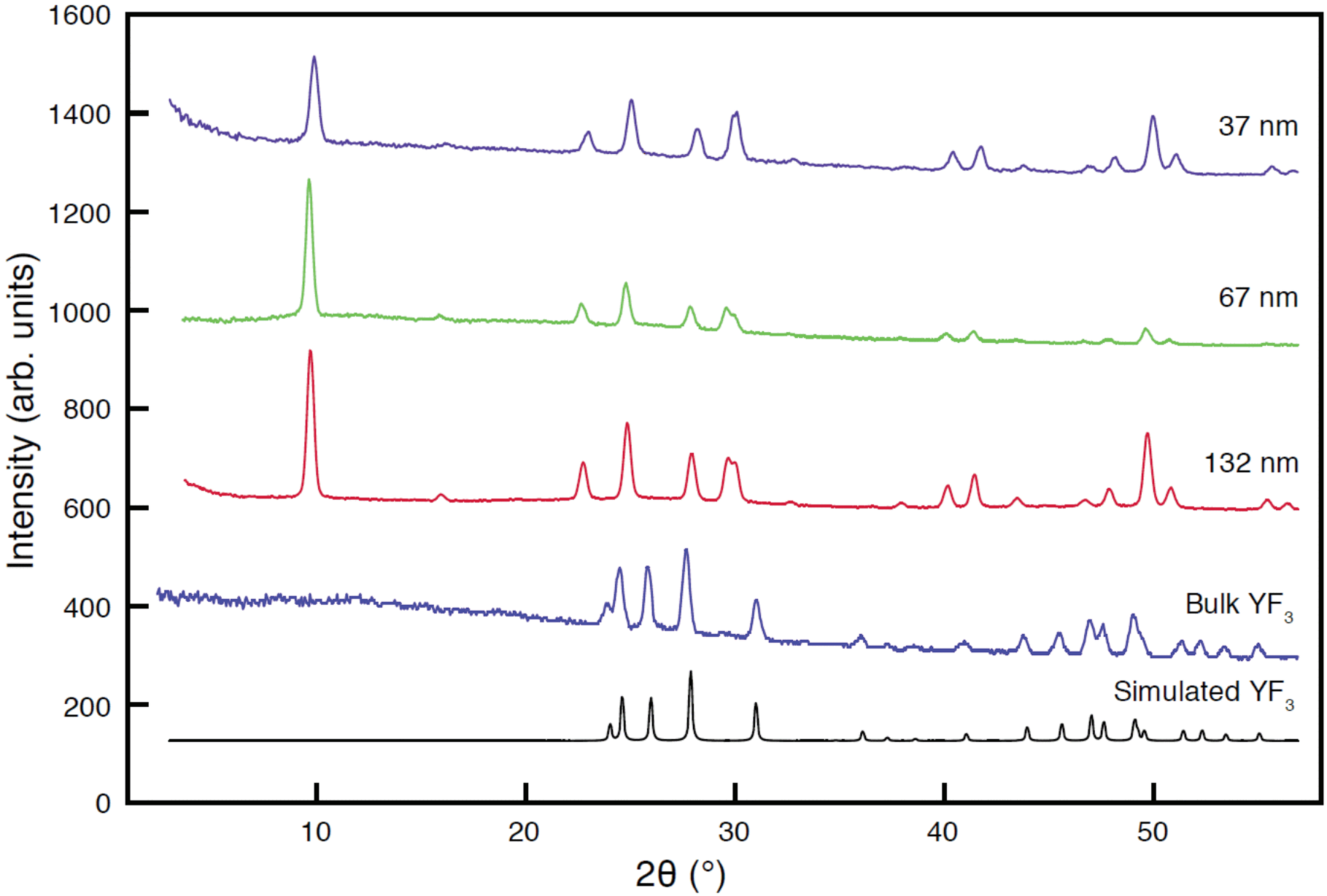

Figure 2. pXRD patterns collected for bulk YF_3 (space group *Pnma*) and $(H_3O)Y_3F_{10} \bullet xH_2O$ nanoparticles, (space group *Fd*-3*m*), with nanoparticle diameters listed in nm. A simulated pXRD pattern for bulk YF_3 is displayed at the bottom.

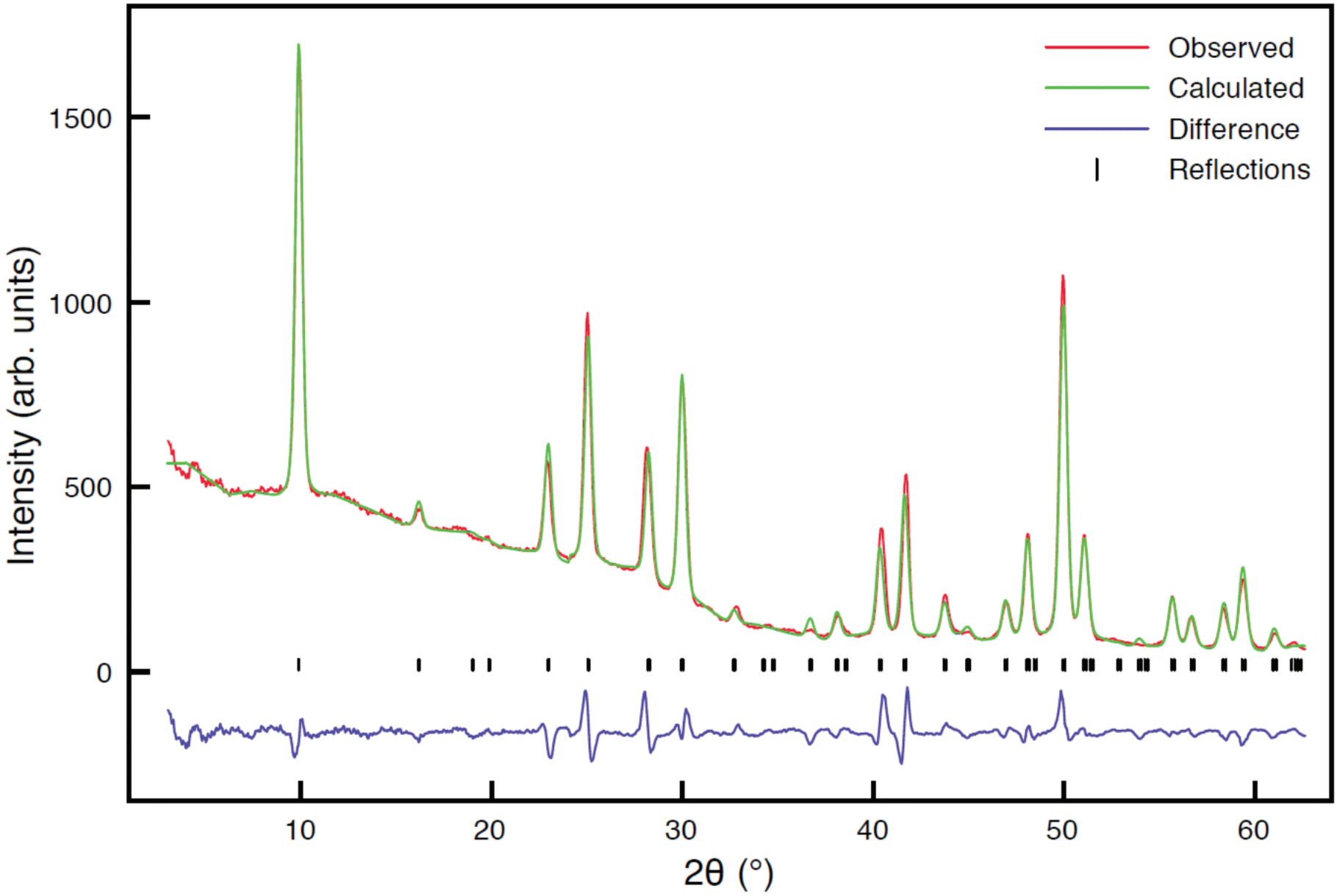

Figure 3. Rietveld profile for the 67 nm diameter $(H_3O)Y_3F_{10} \bullet xH_2O$ nanoparticles using the space group *Fd*-3*m*.

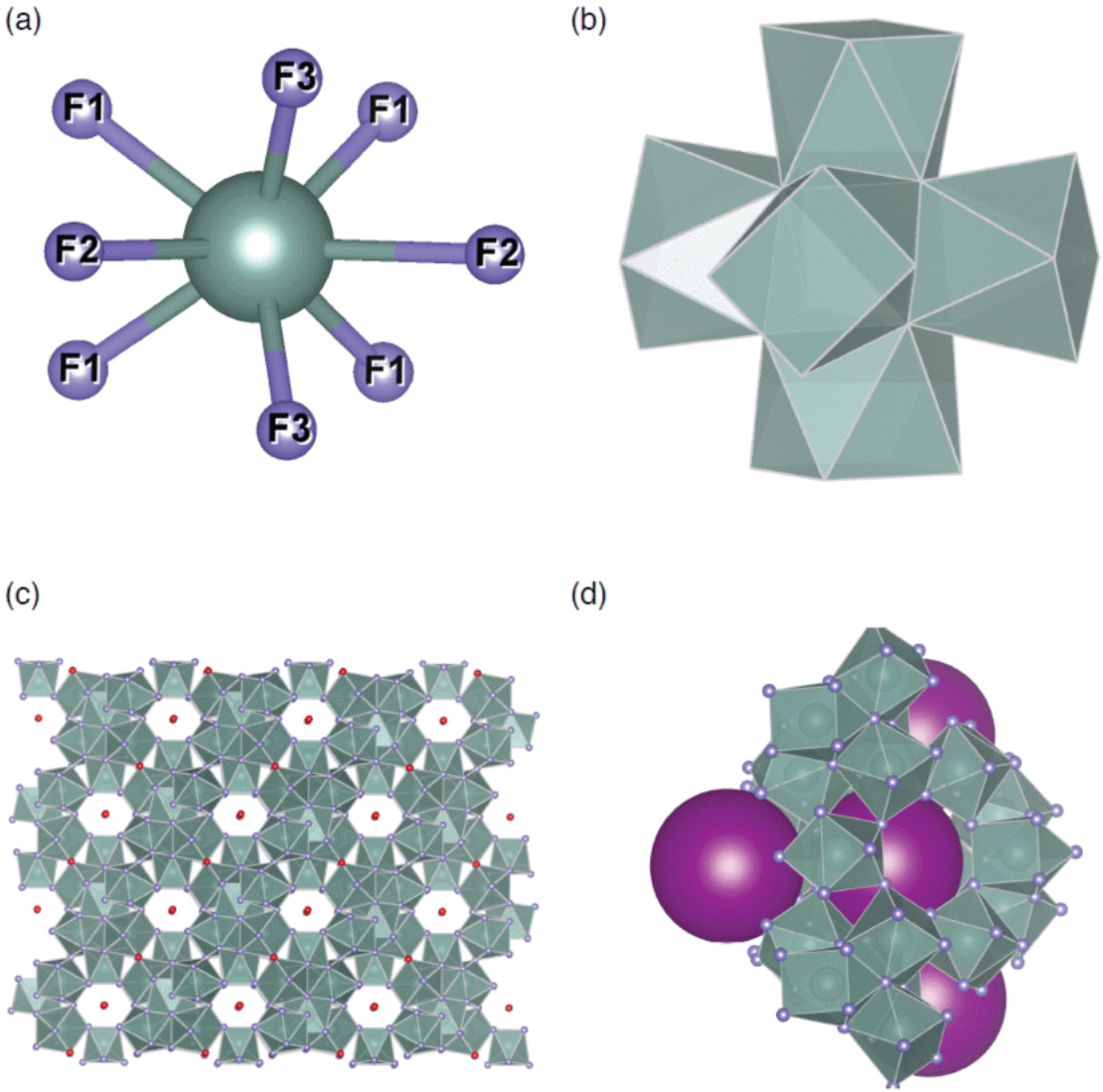

Figure 4. Schematic representation of the $(H_3O)Y_3F_{10}{\cdot}xH_2O$ diamond-like structure where (a) represents the YF_8 coordination polyhedra, (b) represents the $[Y_6F_{32}]^{14-}$ UOA octahedral-like building units, (c) and (d) represent the cage like structure exhibited by the nanoparticles. Fluorine ions are denoted by blue spheres and the yttrium polyhedra are denoted in grey. In (c) the red spheres denote the oxygen ions associated with the H_3O^+ moiety and in (d) the purple spheres indicate the void spaces. The positions of the water molecules within the cages are not shown.

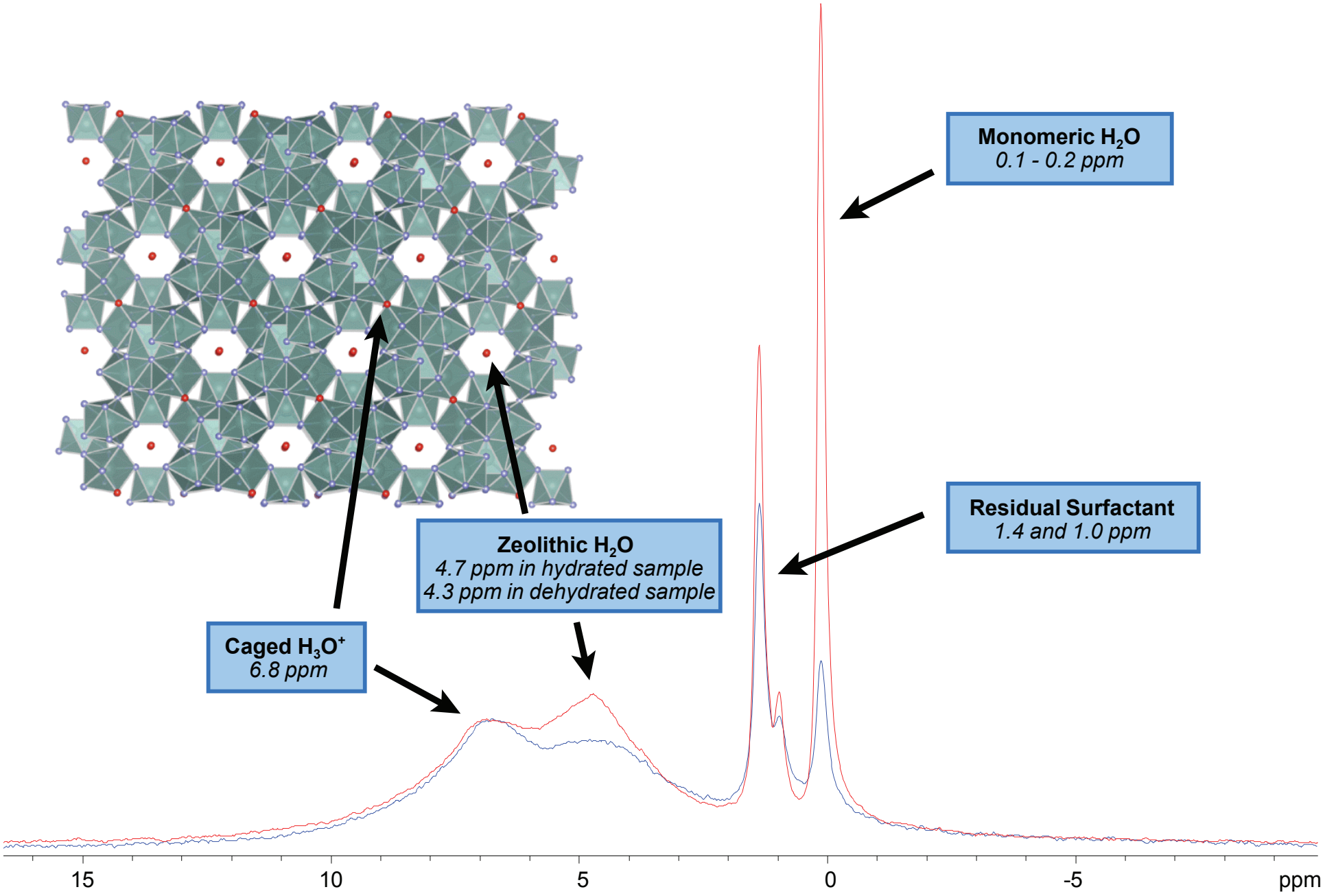

Figure 5. ^{1}H MAS spectra of 67 nm $(H_3O)Y_3F_{10} \bullet xH_2O$ nanoparticles at a spinning speed of 25 kHz. The red trace corresponds to a fully hydrated (x = 1) sample, and the blue trace corresponds to a partially hydrated (x < 1) sample. Inset left: $(H_3O)Y_3F_{10} \bullet xH_2O$ crystal structure.

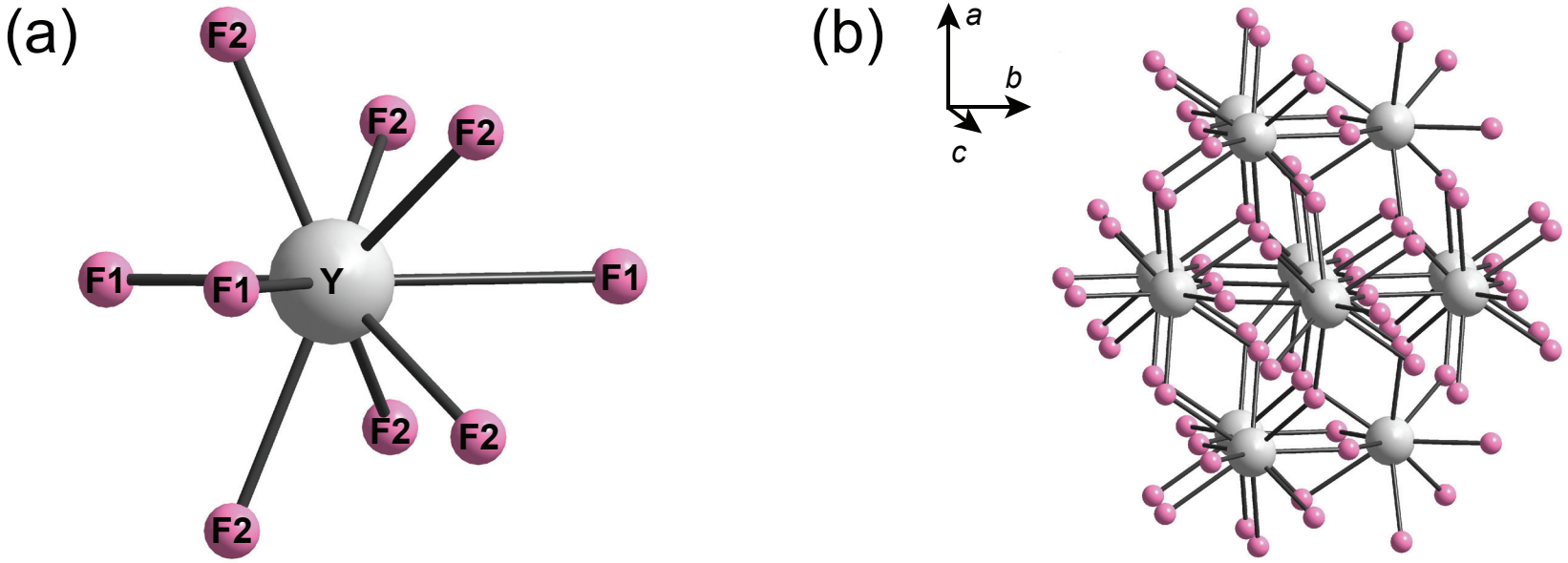

Figure 6. (a) The local nine-coordinate environment about yttrium and (b) the extended structure of bulk YF_3. There are two fluorine sites in a 1:2 ratio and one unique yttrium center.

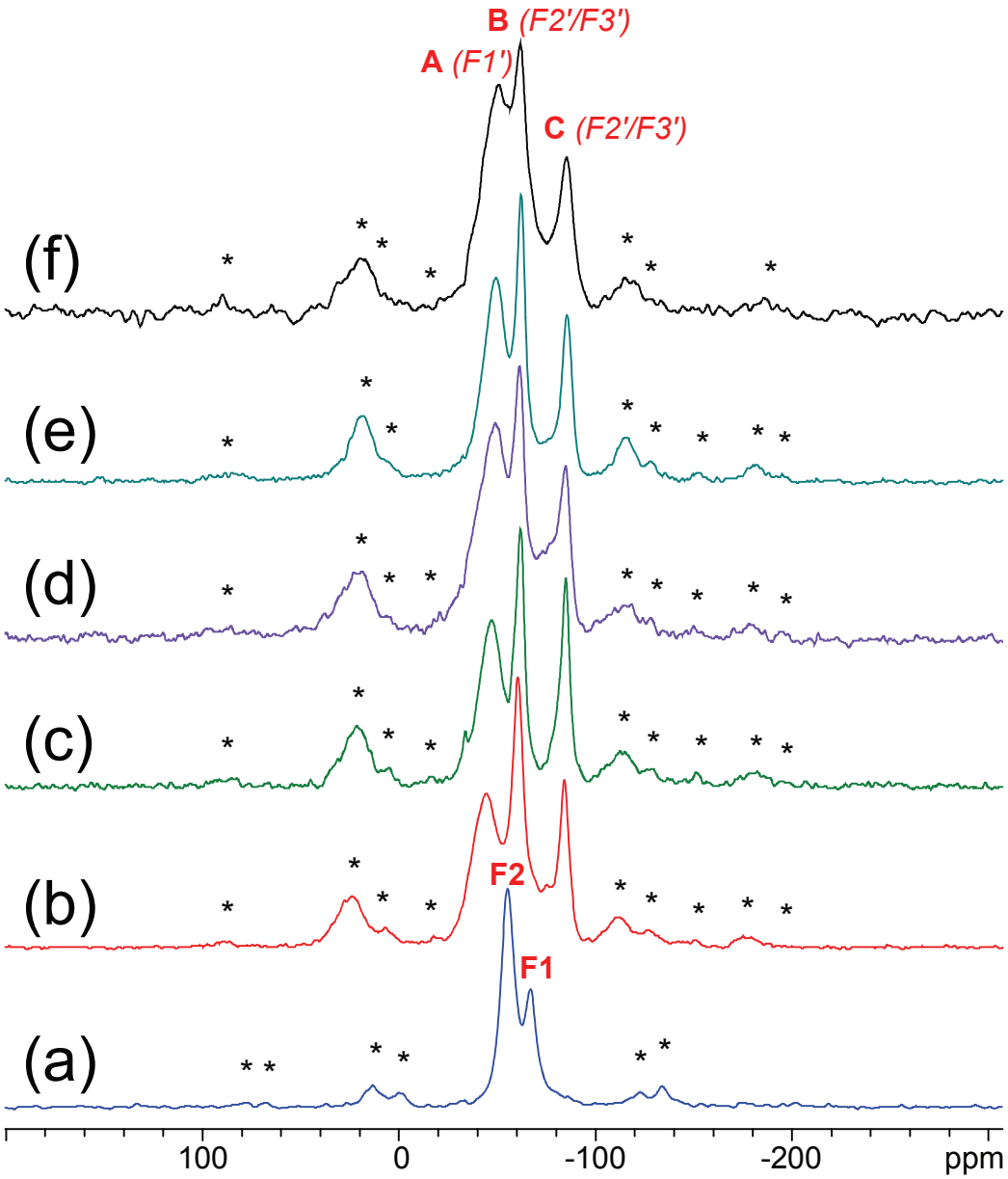

Figure 7. ^{19}F MAS NMR spectra of (a) bulk YF_3 and hydrated $(H_3O)Y_3F_{10} \bullet xH_2O$ nanoparticles of size (b) 132 nm, (c) 67 nm, (d) 49 nm, (e) 37 nm, and (f) 21 nm. Spectra recorded at a spinning speed of 25 kHz. F1 and F2 in (a) denote isotropic chemical shifts in bulk YF_3, A, B, and C for (b)-(f) denote isotropic chemical shifts in $(H_3O)Y_3F_{10} \bullet xH_2O$, while asterisks (*) denote spinning sidebands.

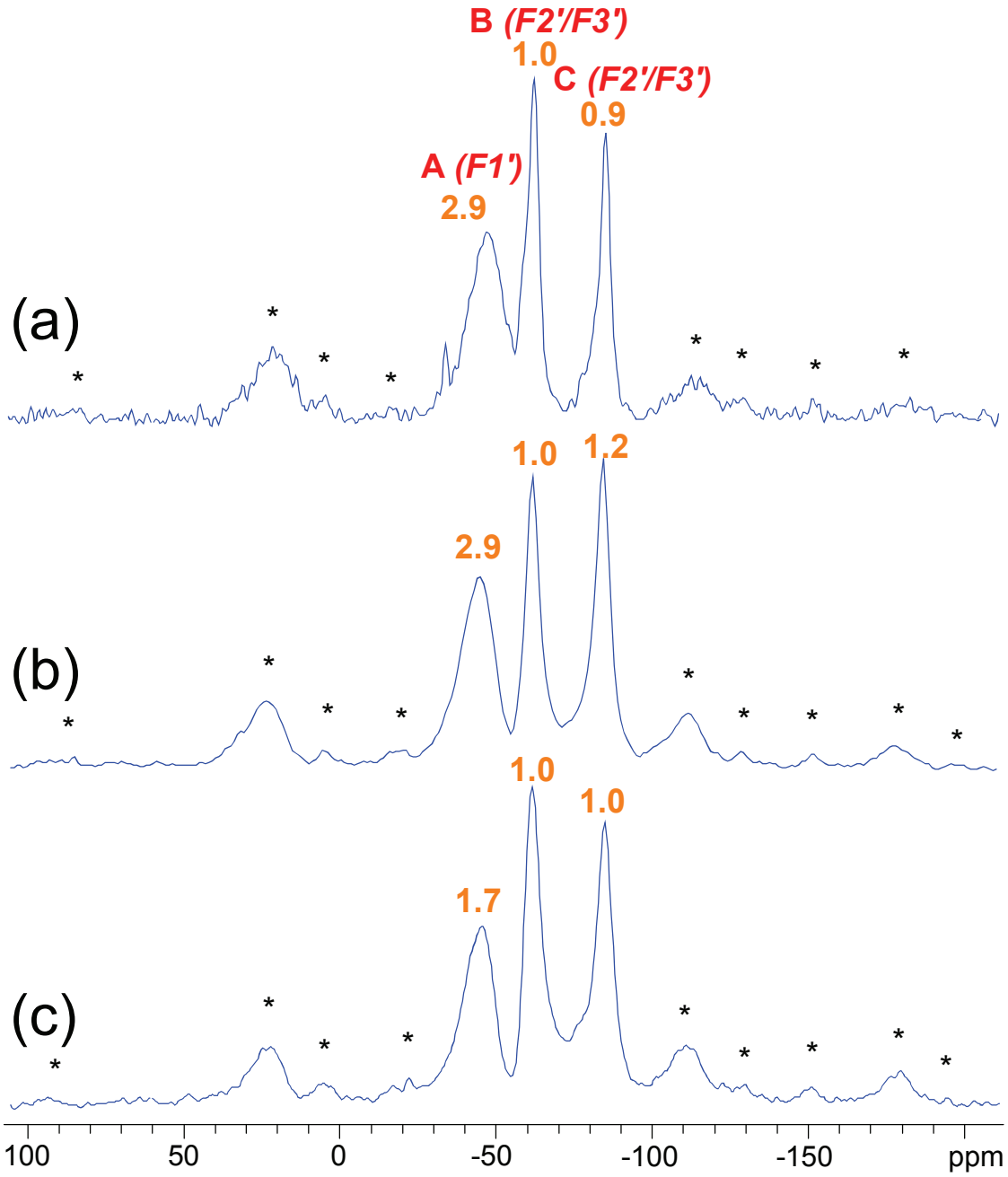

Figure 8. ^{19}F MAS NMR spectra for 67 nm $(H_3O)Y_3F_{10} \bullet xH_2O$ nanoparticles (a) as received (hydrated), (b) after prolonged air exposure (hydrated), (c) after 12 hours of heating at 125 °C (partially hydrated). Spectra were recorded at a spinning speed of 25 kHz. Peak labels indicate resonance assignment and integration ratios (including spinning sidebands). Asterisks (*) denote spinning sidebands.

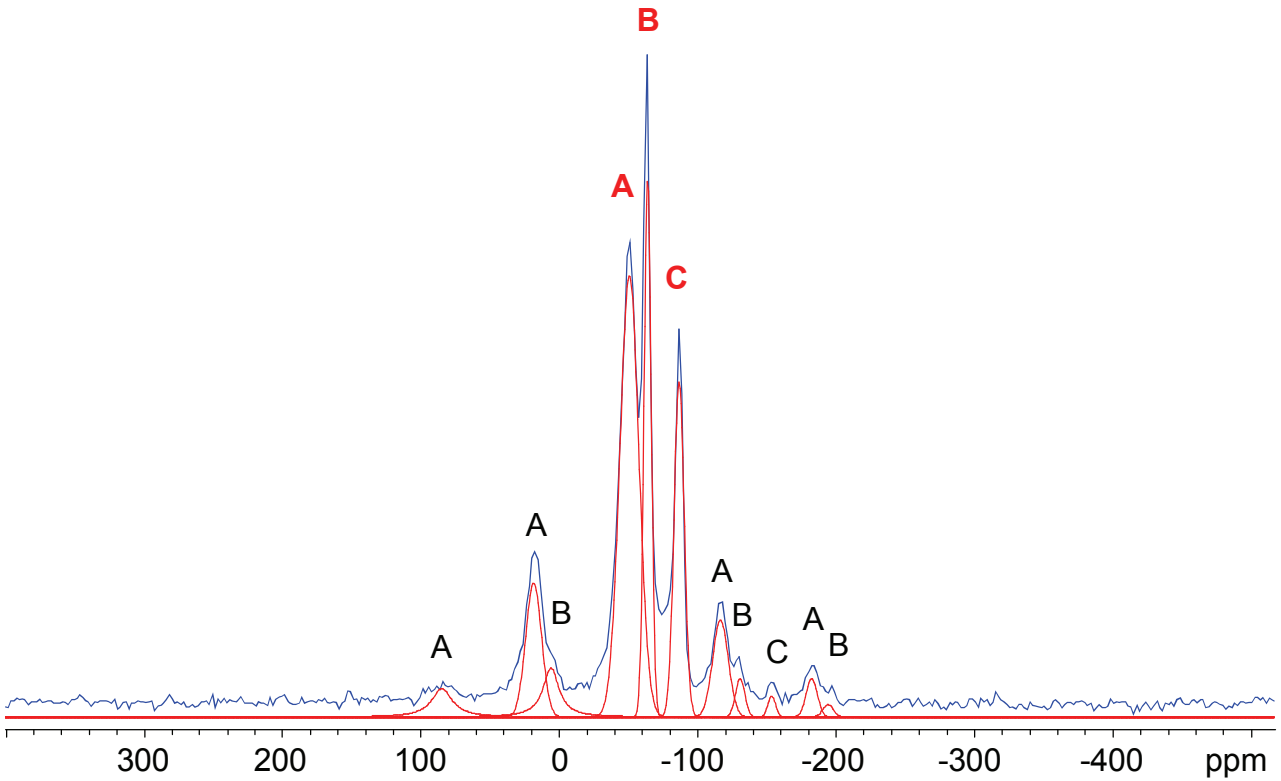

Figure 9. Deconvoluted ^{19}F MAS NMR spectra of hydrated 37 nm $(H_3O)Y_3F_{10} \bullet xH_2O$ nanoparticles. Spinning sidebands are labeled according to the corresponding isotropic peak. Spectra were recorded at a spinning speed of 25 kHz.

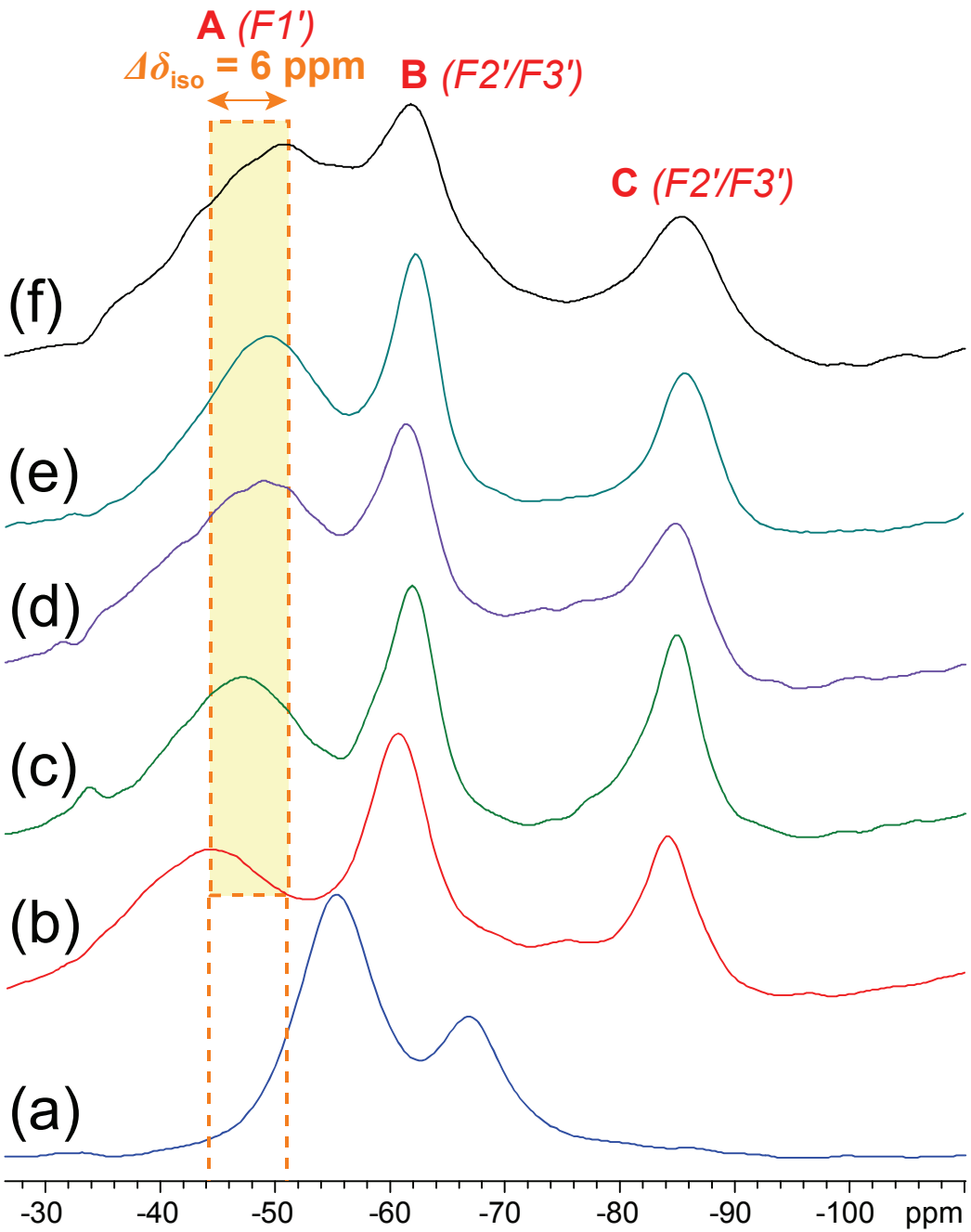

Figure 10. Change in δ_{iso} of resonance A correlated with nanoparticle size in ^{19}F MAS NMR spectra of hydrated $(H_3O)Y_3F_{10} \bullet xH_2O$ nanoparticles of size (b) 132 nm, (c) 67 nm, (d) 49 nm, (e) 37 nm, and (f) 21 nm. Bulk YF_3 is shown in (a) for comparison. Spectra recorded at a spinning speed of 25 kHz. A, B, and C denote isotropic chemical shifts in hydrated $(H_3O)Y_3F_{10} \bullet xH_2O$.

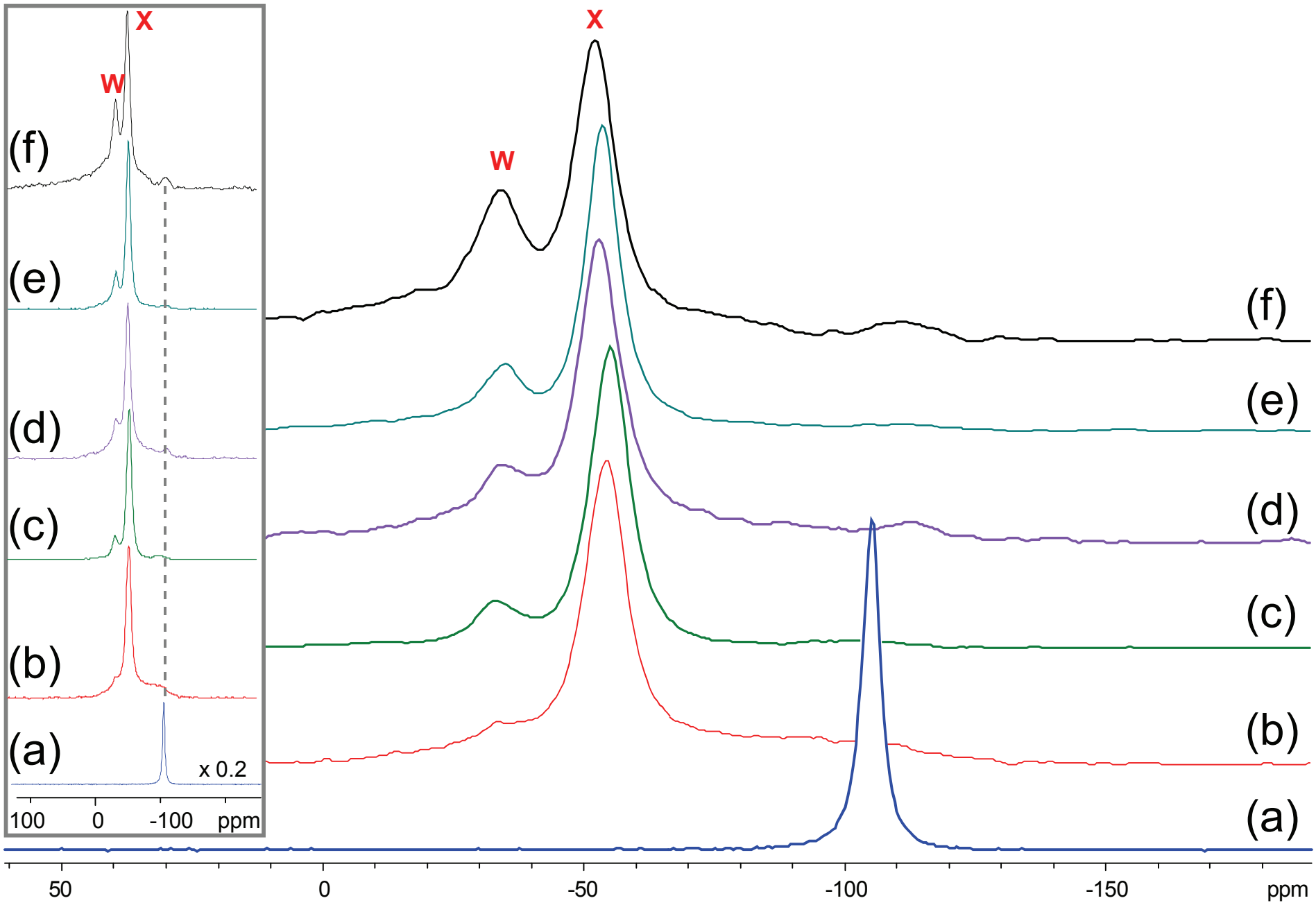

Figure 11. ^{19}F-^{89}Y VACP/MAS NMR spectra of bulk YF_3 (a) and hydrated $(H_3O)Y_3F_{10} \bullet xH_2O$ nanoparticles of size (b) 132 nm, (c) 67 nm, (d) 49 nm, (e) 37 nm, and (f) 21 nm. Spectra recorded at a spinning speed of 5 kHz. Inset left: The dashed grey line indicates traces of bulk YF_3 exist as various degrees of impurity in the $(H_3O)Y_3F_{10} \bullet xH_2O$ nanoparticle samples.

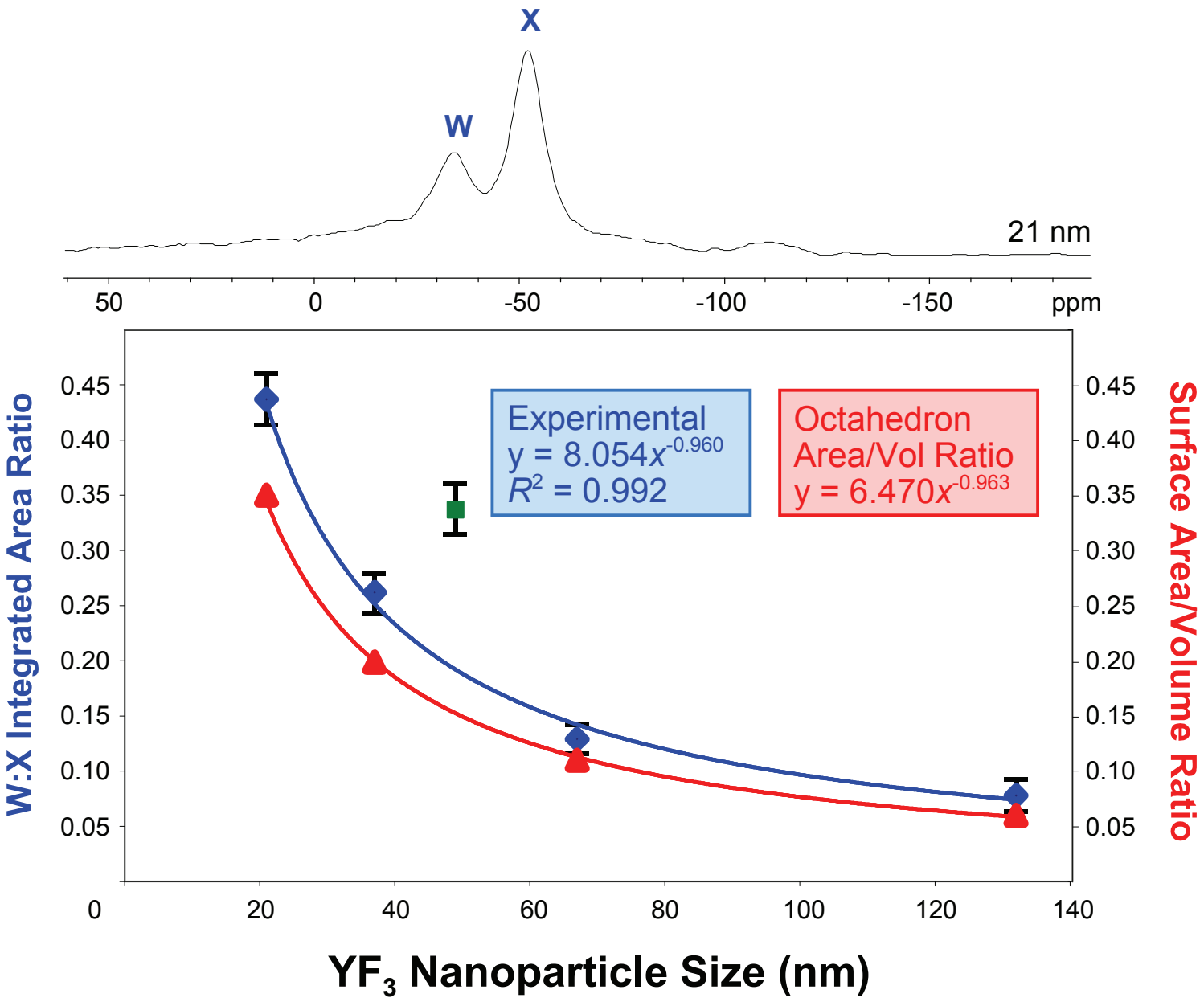

Figure 12. The graph depicts the relationship between the ratio of the integrated areas of **W** and **X** peaks and $(H_3O)Y_3F_{10} \bullet xH_2O$ NP size in ^{19}F-^{89}Y VACP/MAS spectra of hydrated samples. Blue data points represent experimental ratios, red data points represent surface area/volume ratios of ideal octahedra (see Table 6). The green outlier represents the 49 nm Sc-doped $(H_3O)Y_3F_{10} \bullet xH_2O$ nanoparticles.

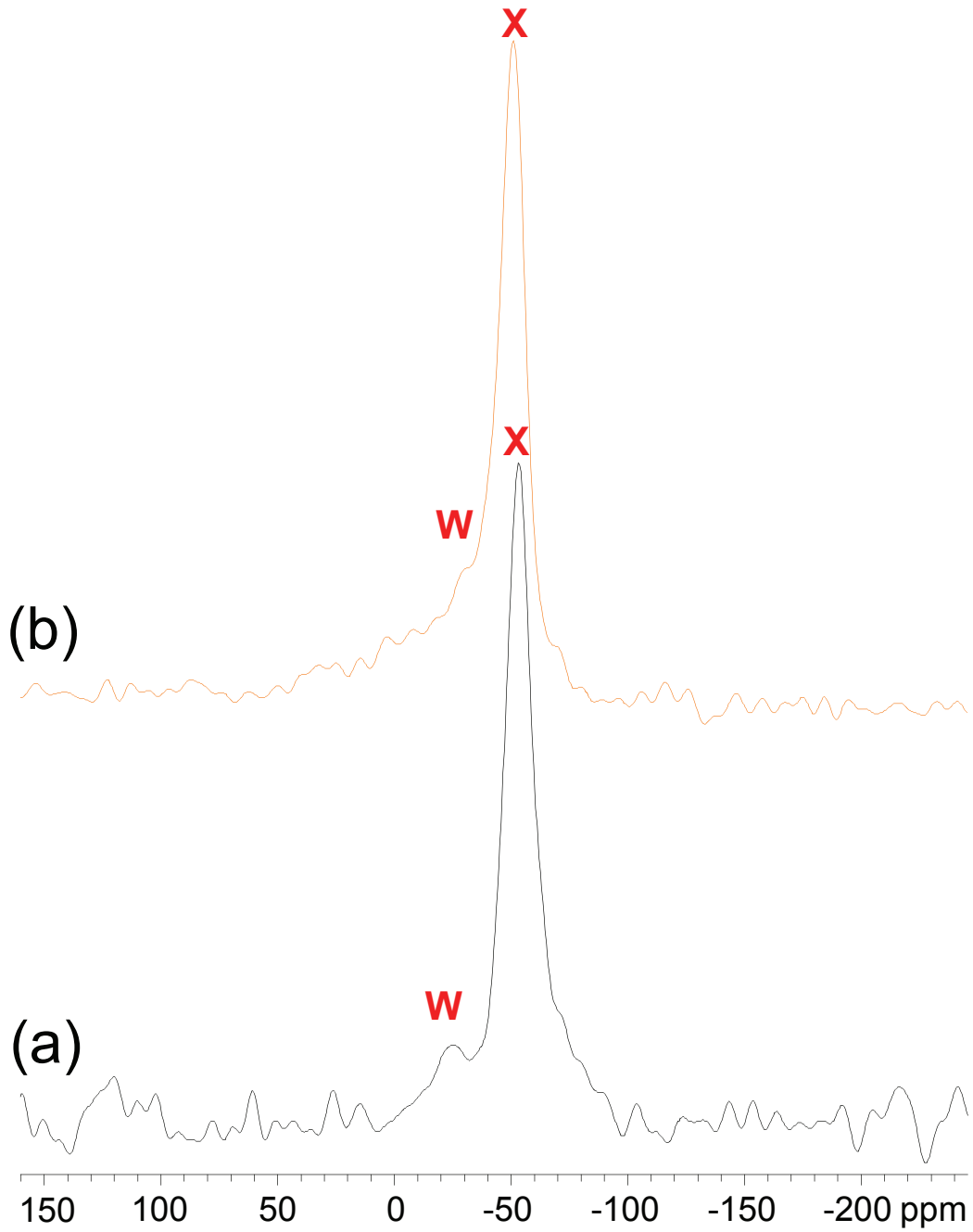

Figure 13. ^{19}F-^{89}Y VACP/MAS NMR spectra of 83 nm $(H_3O)Y_3F_{10} \bullet xH_2O$ nanoparticles, where (a) is a fully hydrated sample, and (b) is only partially hydrated. Spectra were recorded at a spinning speed of 5 kHz.

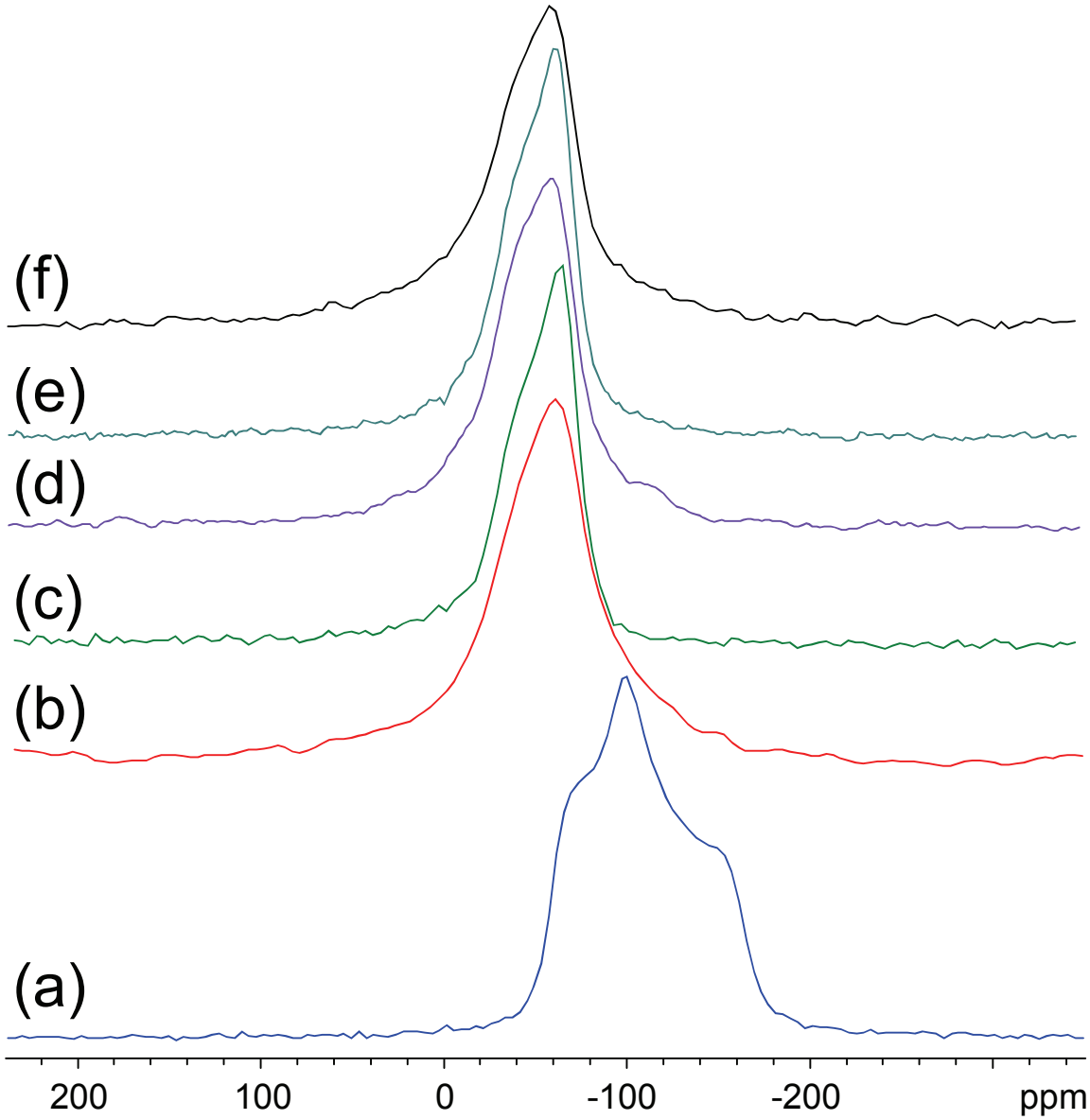

Figure 14. Static ^{19}F-^{89}Y VACP NMR spectra of (a) bulk YF_3 and hydrated $(H_3O)Y_3F_{10} \bullet xH_2O$ nanoparticles of size (b) 132 nm, (c) 67 nm, (d) 49 nm, (e) 37 nm, and (f) 21 nm.

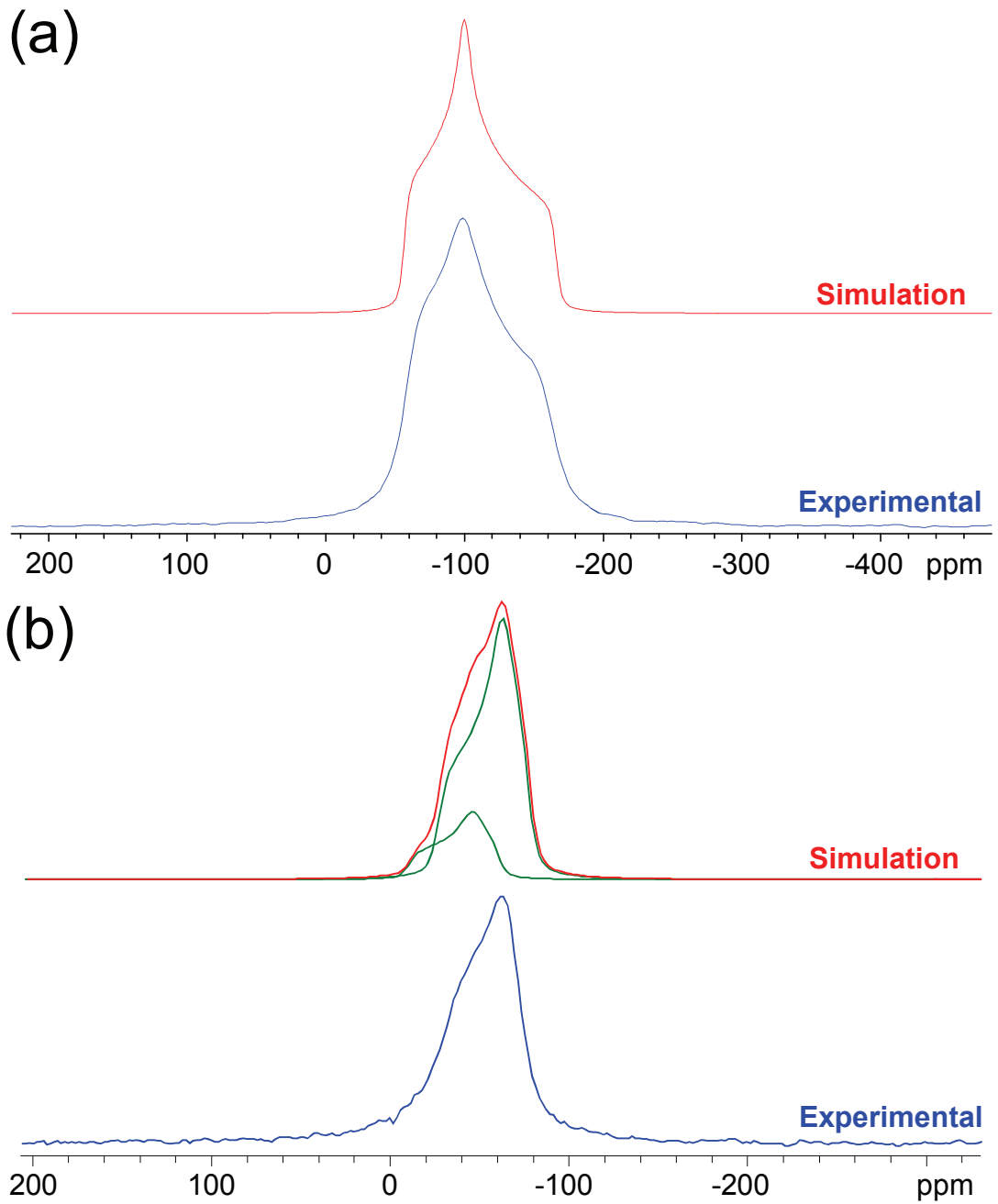

Figure 15. Static ^{19}F-^{89}Y VACP NMR spectra and simulation of (a) bulk YF_3 and (b) hydrated 37 nm $(H_3O)Y_3F_{10} \bullet xH_2O$ nanoparticles. See Table 7.

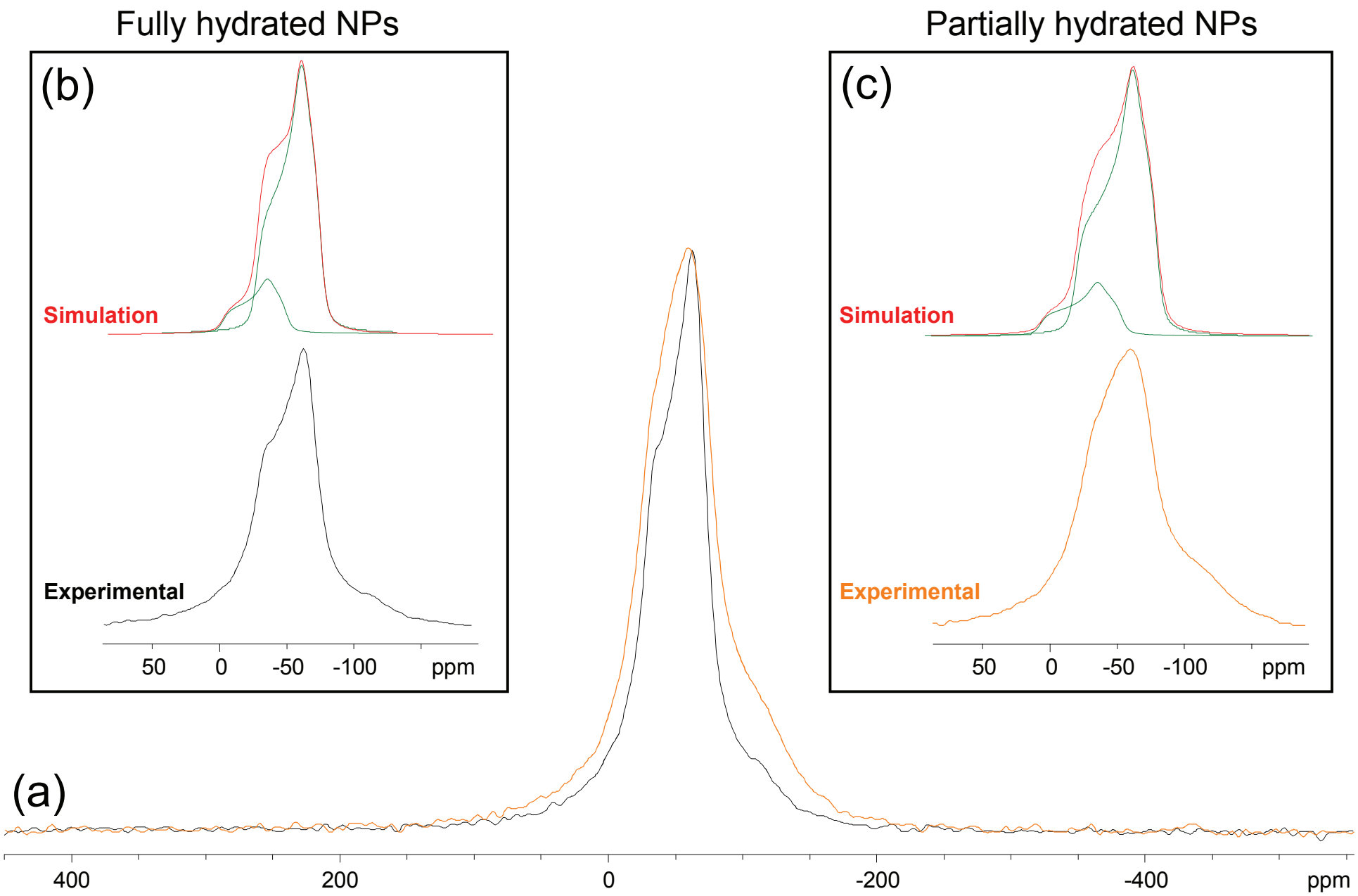

Figure 16. Overlaid static ^{19}F-^{89}Y VACP NMR spectra of fully (black) and partially (orange) hydrated 83 nm $(H_3O)Y_3F_{10} \bullet xH_2O$ nanoparticles are shown in (a). Simulations of spectra of the fully ((b), inset left), and partiallly ((c), inset right) hydrated NPs are also shown. See Table 7.